Materials Advances

ROYAL SOCIETY OF CHEMISTRY

REVIEW

View Article Online
View Journal | View Issue

Cite this: *Mater. Adv.*, 2021, 2, 7187

Photocatalytic reduction of CO_2 by halide perovskites: recent advances and future perspectives

Muhammad Ali Raza,[a] Feng Li,[a] Meidan Que,*[b] Liangliang Zhu*[a] and Xi Chen*[c]

Photocatalytic CO_2 reduction to generate energy-rich fuels through solar energy provides an attractive route to alleviate the global energy crisis and environmental concerns. Searching for various photocatalysts with high catalytic activity and selectivity for the transformation of CO_2 is the key strategy to accomplish this goal. Halide perovskite nanomaterials, with the advancements of facile synthesis, excellent light-harvesting, efficient exciton generation, long carrier diffusion length, and abundant surface sites, have great potential in solar energy conversion. In this review, the fundamental photocatalytic mechanism for CO_2 reduction is firstly highlighted and the impact of the structural properties of halide perovskites is presented. Then, recent advancements of the reaction medium, halide perovskites (*e.g.*, ABX_3 structure and $A_2B'B''X_6$ structure), and their composites (*e.g.*, oxide, sulfide, carbide, metal–organic framework, noble metal, and carbon derivative) as photocatalysts are described and analyzed. Finally, potential research approaches and future perspectives for the improvement of halide perovskite-based photocatalysts toward efficient CO_2 reduction are briefly discussed. This review sheds light on the upcoming innovative photocatalysts for CO_2 reduction into high value-added products.

Received 9th August 2021,
Accepted 4th October 2021

DOI: 10.1039/d1ma00703c

rsc.li/materials-advances

1. Introduction

Tremendous natural environmental changes have made people around the world increase crisis awareness when we are facing unprecedented nature. Great attention has been paid to the depletion of natural resources and the impact of the emission of greenhouse gases on the environment due to the burning of fossil fuels.[1–4] Solar-driven carbon dioxide (CO_2) conversion is an encouraging strategy to alleviate the negative effect of greenhouse gases,[5,6] which uses artificial photosynthesis and

[a] *School of Chemical Engineering, Northwest University, Xi'an 710069, China. E-mail: zhu.liangliang@nwu.edu.cn*
[b] *College of Materials Science and Engineering, Xi'an University of Architecture and Technology, Xi'an 710055, China. E-mail: mdque@xauat.edu.cn*
[c] *Earth Engineering Center, Center for Advanced Materials for Energy and Environment, Department of Earth and Environmental Engineering, Columbia University, New York, NY10027, USA. E-mail: xichen@columbia.edu*

Muhammad Ali Raza

Muhammad Ali Raza received his M.S. in Environmental Engineering from Northwestern Polytechnical University in 2017. Now, he is pursuing the PhD degree at Northwest University, China. His research direction is photocatalytic CO_2 reduction.

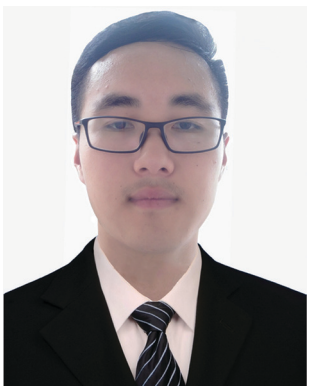

Feng Li

Feng Li is a graduate student at Northwest University, Xi'an, China. His research interests focus on materials and processes for carbon capture and utilization.

photocatalysis of solar energy for carbon feedbacks and is also a straightforward and flexible pathway of CO_2 valorization.[7,8]

Since the landmark breakthrough in 1972, the pioneering work on ultraviolet (UV) driven photocatalytic production of hydrogen by TiO_2[9] has spurred enormous interest and motivated decades of scientific research and progress, which are of particular importance for energy transformation (*e.g.*, reduction of CO_2 and water splitting), chemical transformations, and the decontamination of organic pollutants.[10] During recent years, the rapid increase in the CO_2 concentration in the environment has caused widespread concern.[11] Extensive efforts have been devoted to stabilizing and controlling the concentration of CO_2 in the environment, leading to CO_2 capture and renewable energy production. In particular, the state-of-the-art photocatalytic reduction of CO_2 has been considered as one of the most promising ways.[12]

From the perspective of long-term development, it is essential to explore cost-efficient photocatalysts with outstanding properties and performances. An ideal photocatalytic material should possess wide-range and superior light absorption, effective charge separation, excellent stability and proper redox ability.[13] Upon illumination, the photogenerated charge carriers are produced in the conduction band (CB) and valence band (VB) in semiconductors, respectively. When the energy structure of these semiconductors straddles the redox potentials, their photogenerated charge carriers would involve the surface redox reaction. However, most pure semiconductors (g-C_3N_4,[14] TiO_2,[15] and Cu_2O[16]) as photocatalysts are far from the ideal state yet, because of various limitations, *e.g.*, quick recombination of photo-generated charge carriers, large bandgap, and poor photoreduction potential. Hence, there is still a huge demand to explore low-cost, stable, and effective artificial photocatalysts for CO_2 fixation.

Recently, halide perovskites have drawn enormous attention by virtue of their excellent photoelectric properties, for example, long charge carrier diffusion length, adjustable bandgap, high absorption coefficient, and excellent external quantum efficiency.[17–21] Due to these impressive characteristics and attractive properties, halide perovskites have been extensively employed in the fields of photoelectric conversion,[22] reduction reaction of CO_2, and hydrogen evolution reaction.[23–27] These successful applications also encourage more applications in other traditional fields.[28] Recent developments in the synthesis methods (*e.g.*, hot-injection, ligand-assisted reprecipitation scheme, ultrasonic method, solvothermal method, microwave assisted method, and ball milling)[29–35] have promoted halide perovskites marching to practical usage.[36] Through controlling the production method, reaction temperature, capping ligand, and additional reaction conditions, halide perovskites with variable chemical components (*e.g.*, inorganic, organic, and inorganic hybrid), dimensions, sizes, and morphologies can be obtained.[37–41] These efforts are expected to bring new opportunities for halide perovskites in the application of photocatalysis.

Halide perovskites have recently attracted great attention towards the reduction of CO_2 into high value-added products, from basic and theoretical research to applied science.[42–52] Shown in Fig. 1 is a timeline of the development of halide perovskites as photocatalysts for CO_2 reduction.

Up to now, there have been some review works of halide perovskites as photocatalysts focusing on the stability issues, or

Meidan Que

Meidan Que is currently working as an associate professor at Xi'an University of Architecture and Technology in China. She got her PhD at Xi'an Jiaotong University in 2018 working on optical materials for perovskite solar cells. From Sep. 2017 to Sep. 2018, she studied as a visiting scholar at Brown University. Currently, her research interests focus on semiconductor quantum dots for photovoltaic systems and nanocomposites for photocatalyst applications.

Liangliang Zhu

Liangliang Zhu is working as an associate professor at the School of Chemical Engineering of Northwest University, Xi'an, China. He received his PhD degree from Xi'an Jiaotong University, Xi'an, China, in 2018. His research interest is in multi-scale materials for carbon capture and utilization, and flexible structures.

Xi Chen

Xi Chen is a professor at the Department of Earth and Environment Engineering at Columbia University. He is the Director of the Earth Engineering Center, and the Center for Advanced Materials for Energy and Environment at Columbia University. He received his PhD from Harvard University in 2001 and joined Columbia in 2003. He has received numerous awards including the Presidential Early Career Award for Scientists and Engineers (PECASE), ASME Sia Nemat-Nasser Early Career Award, and the SES Young Investigator Medal.

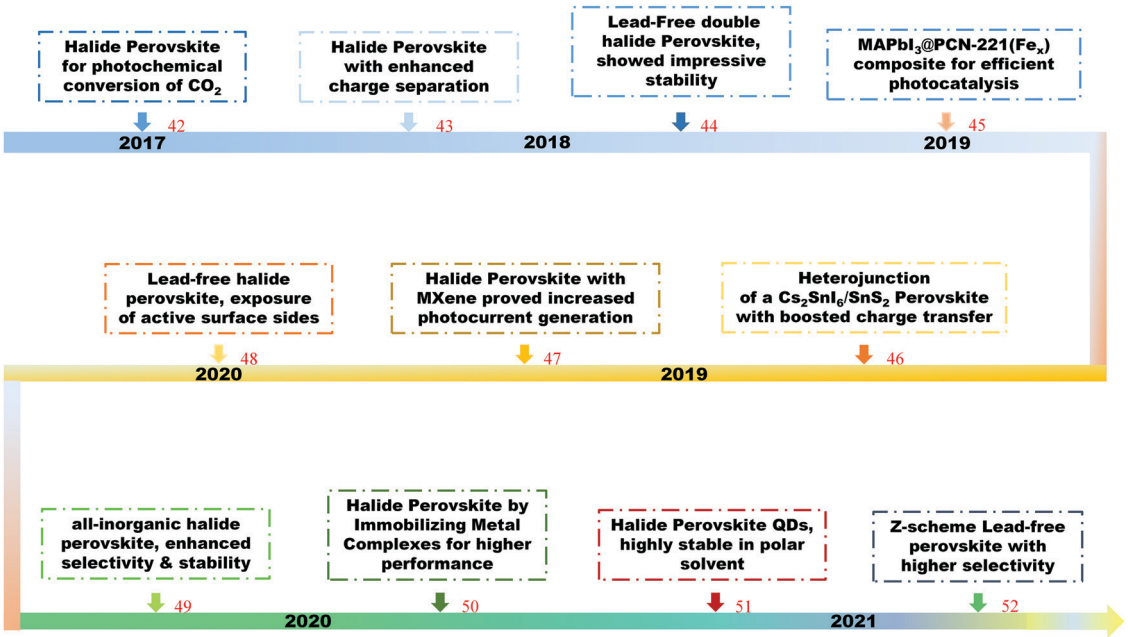

Fig. 1 The development of halide perovskites as photocatalysts for CO_2 reduction.

modification strategies through structural engineering and interfacial modulations.[53–57] However, a timely and comprehensive review is still in demand concerning the photoreduction mechanism, reductants and products, the structure and photocatalytic performances, and the exploration efforts on halide perovskites and their composites for further improvements. In this review, we start with the basic mechanism of the photoreduction of CO_2, and the reductants and products. After that, the fundamental photoelectrical properties of halide perovskites are described collectively, including their crystal structure, defect tolerance, toxicity, luminescence properties, and photostability issues. Insights into the molecular calculations of halide based perovskites concerning their unique electronic structure and physio-chemical properties are also included. Then, we summarize the existing exploration efforts on halide perovskites and their composites in tuning the selectivity of photocatalytic reduction of CO_2 as well as increasing the active sites. Finally, we present the outlook for upcoming directions and the great potential of halide perovskites toward photocatalytic CO_2 reduction.

2. Photocatalytic mechanism for CO_2 reduction

In the process of photocatalysis, the abundantly available solar energy is transformed into electrical/chemical/thermal energies through semiconductor materials.[13,58–61] In general, the photocatalysis process for CO_2 reduction mainly consists of three critical synergistic steps, as illustrated in Fig. 2. In the first step, photon absorption occurs to create electron–hole pairs. During this catalytic reaction, incident light induces the transition of electrons from the valence band (VB) to the conduction band (CB), leaving an equal number of holes in the VB. A suitable band structure of the photocatalyst is required to reduce CO_2 or oxidize water. However, in the second step, a large number of fractions of photogenerated electron–hole pairs may be consumed by recombination. The recombination is dominant over charge separation or *vice versa*, depending on the relative time scale among the rate of recombination and photogenerated carriers. This issue can be resolved *via* a very complex interaction among dimension, surface properties, material crystallinity, and several other structural factors. The design of balanced active sites was utilized to facilitate charge separation. The final step is the CO_2 adsorption. This redox reaction involves the transfer of electrons from the photocatalyst to CO_2 molecule. In general, larger surface area of the photocatalyst can lead to higher rate of CO_2 adsorption thanks to more active sites.[62–64] The photocatalytic activity is generally associated with two main conditions: (i) the

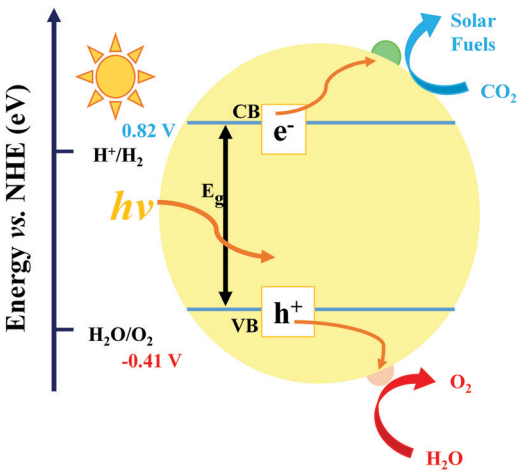

Fig. 2 Schematic diagram of the photocatalytic CO_2 reduction mechanism.

bandgap energy (E_g) of the photocatalyst should be lower than the energy of the incident light ($h\nu$; the absorption energy). (ii) The reduction potential of the reacting species should be positioned between the CB and VB values of the photocatalyst material. The former condition specifies a narrower bandgap that can help the effective utilization of incident photons. Conversely, the latter condition reveals that a higher value of CB potential and a lower value of VB potential are thermodynamically advantageous toward the reduction as well as oxidation reactions of the reacting species, respectively. Therefore, it is inevitable to seek the balance point owing to the existence of the noticeable inconsistency as discussed in the above conditions. However, this is quite a challenging task to obtain both broad light absorption and robust redox capability simultaneously for pure component semiconductor materials. Moreover, the photogenerated electrons in the CB can easily recombine with holes, or be trapped in the defect state, or easily come back to the VB for a pure-component material, which would decrease the efficiency of solar energy utilization.[65] Hence, designing a suitable heterogeneous photocatalyst is an effective approach to overcome the above-mentioned issues. Generally, there are four vital rules played by cocatalysts: (i) enhancing the separation and transfer of charges, (ii) boosting the performance, and the selectivity of photoreduction of CO_2, (iii) improving the durability of photocatalysts in a peculiar environment (*e.g.* high humidity and high temperature), and (iv) suppressing the side reactions (*e.g.*, H_2 reduction).

Photocatalytic reduction of CO_2 with a semiconductor-based cocatalyst is affected by many aspects, for example, photocatalyst loading, particle size, structure, composition, dispersion, crystal facets, alloy phase, morphology, and valence states. In a photocatalyst system, the maximum photocatalytic performance is accomplished at an optimum loading of cocatalysts. An additional loading of the cocatalyst may lead to deterioration of catalytic activity owing to the following factors. (i) Too much cocatalyst can hinder the incident light and reduce the light absorption ability, hence decreasing the photogenerated electron–hole pairs. (ii) Excessive cocatalyst percentage could in turn shield the active sites on the surface of the photocatalyst, therefore lessening the contact with H_2O and CO_2 molecules. (iii) Excessive loading may cause the irregular dispersion and formation of bigger particles, consequently reducing the catalytic performance.

A closed gas circulation reactor is usually used for photoreduction of CO_2, where the responded CO_2 decreased in the existence of semiconductors under continuous illumination.[66–71] Since the Gibbs free-energy (ΔG) value for the reduction reaction of CO_2 to produce carbon monoxide (CO) is $\sim$258.95 kJ mol^{-1}, the bandgap of no less than 1.35 eV is needed. Then rapid separation and transfer of the photogenerated charge carriers to the particular catalytic active sites of the photocatalysts triggers the electrochemical reaction, resulting in chemical fuel. For photocatalytic reduction of CO_2 in the existence of water, the CB must be negatively paralleled to the reduction potential of CO_2 (-1.07 V *vs.* normal hydrogen electrode (NHE)) for CO_2 reduction to CO at pH = 0. Simultaneously, the VB should be larger than the oxidation potential of water (1.23 V *vs.* NHE at pH 0) to procedure O_2. Fig. 3 displays the schematic representation of the bandgap and band position of reported typical halide perovskite materials and CO_2 reduction potential.

Photocatalytic CO_2 reduction reaction is a high energy-driven process, because of the carbon-based compound that has a thermodynamically stable and high bond energy of C=O (750 kJ mol^{-1}).[72,73] Therefore, the photocatalytic reduction reaction of CO_2 also needs prior activation. The process of mass transfer of reactants, CO_2 adsorption and creation of active sites for CO_2 reduction can be improved by increasing the surface area of a photocatalyst. A large number of nanostructured materials for the photocatalyst were developed to achieve larger surface areas, including zero dimensional (0D) nanoparticles,[74] one dimensional (1D) nanowires/nanotubes,[75] two dimensional (2D) nanosheets,[76,77] and three dimensional (3D) hierarchical nanostructures.[78] Furthermore, various porous and hollow materials were extensively studied for CO_2 conversion because of their increased surface area and porosity. The adsorption and activation of CO_2 can also be facilitated by tuning the surface defects of photocatalysts, which can be quite helpful in improving the reactivity and photochemical properties of the photocatalytic processes.[79,80] Strongly negative reduction

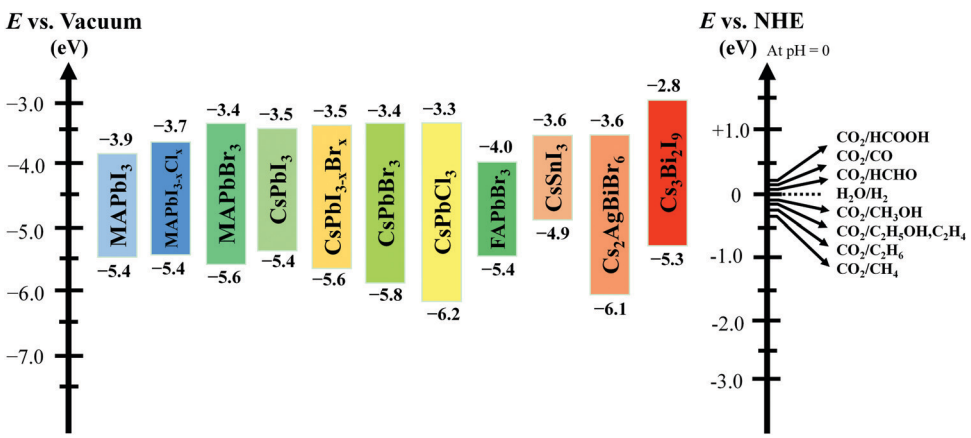

Fig. 3 Conduction and valence band position of halide-based perovskite materials with relative CO_2 reduction potential.

Table 1 CO_2 reduction processes at different reduction potentials, E^0 (V *vs.* NHE at pH = 7)[81,86–88]

Equation	Product	E^0 (V)
$CO_2 + 1e^- = CO_2^{\bullet -}$	Carbonate anion radical	−1.90
$CO_2 + 2H^+ + 2e^- = HCOOH$ (aq)	Formic acid	−0.61
$CO_2 + 2H^+ + 2e^- = CO$ (g) + H_2O	Carbon monoxide	−0.53
$CO_2 + 4H^+ + 4e^- = HCHO$ (aq) + H_2O	Formaldehyde	−0.48
$CO_2 + 6H^+ + 6e^- = CH_3OH$ (aq) + H_2O	Methanol	−0.38
$CO_2 + 8H^+ + 8e^- = CH_4$ (g) + H_2O	Methane	−0.24

potential is required for the activation of CO_2, which occurs on the surface of photocatalysts by the chemisorption method to convert a linear molecule to bend carbonate anion radical ($CO_2^{\bullet -}$) *via* mono- or bi-dentate coordination. Hence, this reactive carbonate anion is the critical factor for various photoreduction of CO_2. To create chains of hydrocarbons, more reactive $CO_2^{\bullet -}$ species can promote reactions *via* two different ways (carbene and formaldehyde), as illustrated in Table 1.[81] However, the obtained products are methane (CH_4) and the formation of some additional products (C_1–C_3 hydrocarbons) in the photocatalytic reduction of CO_2. Hori *et al.* suggested the conversion tracking of CO_2 to CO by reactive $CO_2^{\bullet -}$, and subsequently the reaction with a proton.[82] For the photocatalytic CO_2 reduction reaction, the selectivity of product formation is still challenging and relies on several factors, such as reaction intermediate, and active sites of the photocatalysts. The release of protons initiates these reactions in the presence of water vapor, H_2, or in both cases. These above-mentioned protons form different reduction products after reaction with CO_2 in the existence of photogenerated electrons. The efficiency of the photoreduction process of CO_2 can be shown in terms of product formation rate and the conversion rate of CO_2.[83] CO_2 reduction starts with the formation of new carbon bonds by the cleavage of the O═C═O bond. Photocatalytic reduction of CO_2 is a proton-assisted multielectron reduction process that comprises various intermediate steps as shown in Table 1, for obtaining high-value products (*e.g.*, CO, formic acid, methane, and methanol).[84,85]

3. Crystal structure property of halide perovskites

3.1. ABX_3 structure

Halide perovskites employed by photocatalytic CO_2 reduction facilitate band alignment with the CB position and hinder the photogenerated charge carriers from undergoing recombination. For achieving the higher productivity and selectivity of halide perovskite nanocrystals (NCs) for photoreduction of CO_2, fundamental understandings of the relationships between the structure (chemical composition as well as morphology) and CO_2 selectivity need to be determined.[89] In this section, the impact stemming from halide perovskites from the unit cell will be reviewed. The unit cell is the simplest and smallest volume of a material. The properties of materials derive from special characteristics of the unit cell, *e.g.*, the bond angle, bond length, and symmetry. Moreover, the diffusion lengths and lifetimes of charge carriers in optoelectronic materials are more affected by crystal boundaries and crystal defects.

One of the main chemical formulas of halide perovskites can be symbolized as ABX_3, where A and B represent two different kinds of cations and X represents a halide anion (*i.e.*, Cl, Br, and I). Cation B restricts at the median of the octahedron body composed of six halide anions (Fig. 4a).[90–92] Conventionally, A and B are cations with 12- and 6-fold coordination with X anions at the corner in ABX_3 halide perovskites (Fig. 4a), respectively.[93–95] Recently, various high-performing perovskite materials were developed with A being formamidinium (FA), methylammonium (MA), or Cs; B being Pb, Bi, or Sn; and X being Cl, Br or I.[93–106]

When A site is employed with higher organic cations, low-dimensional halide perovskite structures may form, where the inorganic network connectivity has degenerated to 2D sheets, 1D chains, or 0D clusters (Fig. 4b).[107] Conversely, the crystal symmetry will reduce and the cubic structure is distorted. In bulk lead halide perovskites, three polymorphs are usually noticed: cubic, tetragonal, and orthorhombic phases in the order of decreasing symmetry (Fig. 4a).[92] At higher temperatures, the more stable phase is the cubic phase, and the temperature of phase transitions is clearly defined. For NCs, surface effects may regulate the relative stabilities of several polymorphs, which gains limited attention. All as-synthesized lead halide perovskite NCs crystallize into three-dimensional (3D) phases as follows: $MAPbI_3$ NC is tetragonal; $FAPbBr_3$, $FAPbI_3$, and $MAPbBr_3$ NCs are pseudocubic; and $CsPbI_3$ and $CsPbBr_3$ NCs are orthorhombic at room temperature.[92] One of the most significant features of halide perovskites is their higher tolerance for defects. The nature of halide perovskites is defect-tolerant generally owing to their electronic band structure, where the VB maximum is mostly composed of an anti-bonding orbital,[108–110] and the CB minimum becomes stabilized *via* the strongest spin–orbit coupling. Such defect tolerance behavior involves the conservation of a pristine E_g upon the formation of typical defects, due to their defect energy levels residing entirely in either the VB or CB, rather than within the E_g itself. The large hollow between octahedra (A-site) is preoccupied through one or a combination of three big cations ($CH(NH_2)^{2+}$, $CH_3NH_3^+$, or Cs^+), yielding generally the structure of ABX_3. The tolerance factor calculated by $t = (R_A + R_X)/\sqrt{2}(R_B + R_X)$, where R_A, R_B, and R_X are the ionic radii of the corresponding ions, should be near 1 to keep a higher symmetry cubical structure of the perovskite. Fig. 4c presents the tolerance factors for the best widespread Pb or Sn halide perovskites. Due to the larger numbers of Pb or Sn atoms occupying the B sites of halide perovskites, the A site must be larger enough to placate the tolerance factor.[111]

3.2. Luminescence properties

Halide perovskite NCs have excellent luminescence without advance electronic surface passivation. Protesescu *et al.* presented nearly ideal photoluminescence efficiency from colloidal $CsPbBr_3$ NCs.[32] The composition of lead halide perovskite NCs can be appropriately adjusted through cation or anion exchange, as shown in Fig. 5a.[38] The photoluminescence spectra of lead halide perovskite NCs span the whole visible light range and their peak

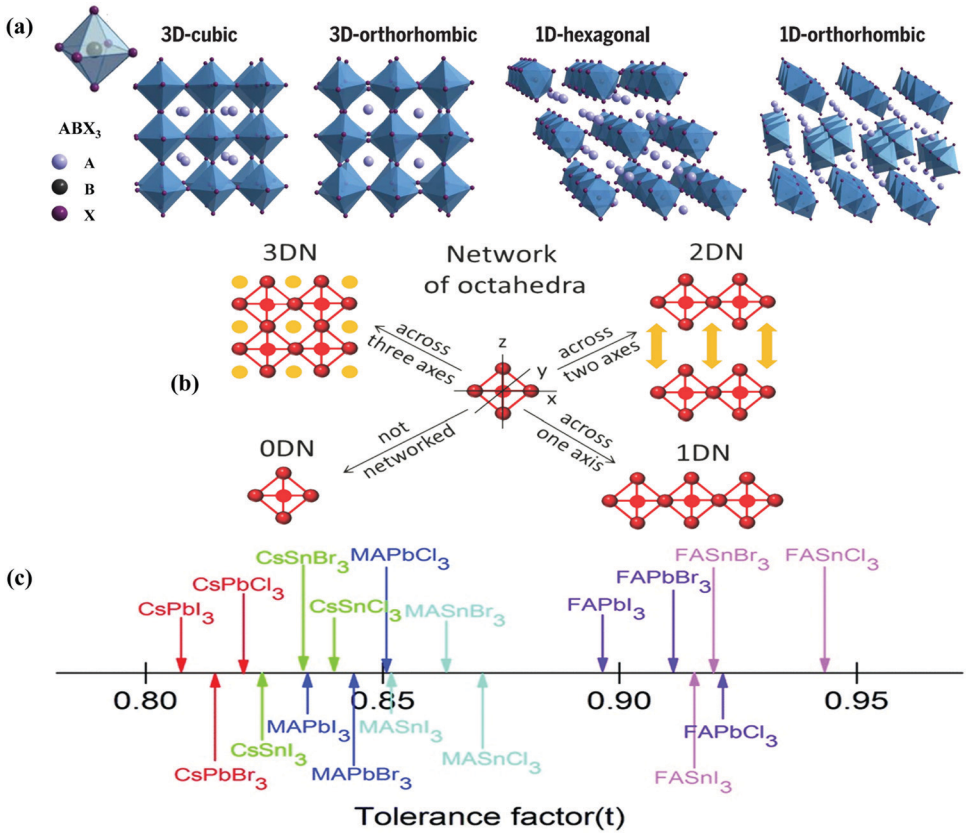

Fig. 4 Structures and physical properties of halide perovskites. (a) Crystal structure of 3D-cubic, 3D-orthorhombic, 1D-hexagonal, and 1D-orthorhombic phases. From ref. 92, reprinted with permission from AAAS. (b) Schematic structural diagrams of the change network of octahedra. Reproduced with permission from ref. 107 at https://pubs.acs.org/doi/10.1021/acsenergylett.6b00705; further permissions are directed to the ACS. (c) Tolerance factor of ABX_3 halide perovskites. Republished with permission of the Royal Society of Chemistry, from ref. 111; permission conveyed through Copyright Clearance Center, Inc.

positions are tunable through modifying the composition (Fig. 5b), size, and shape.[92] Higher photoluminescence quantum yield with tunable emission, low costs, and simple synthesis of halide perovskite NCs make them appealing in practical applications. However, the toxicity of lead, sensitivity to the atmosphere condition (humidity, oxygen, daylight, and temperature), and limited yield still hamper further photocatalysis application of lead-based halide perovskite NCs. Halide perovskites have great photophysical properties, including high absorption coefficients, low trap densities, long charge diffusion lengths, and broadly tunable bandgaps. These properties allow for light-harvesting from ultra-visible to the near inferred spectral range.[46,112] Besides, the band positions of halide perovskites mostly fulfill the thermodynamic requirements for photocatalytic reduction of CO_2.[113]

3.3. Other structures

The lead halide perovskite-based NCs with a 3D $APbX_3$ crystal structure and composition have become the focus of much

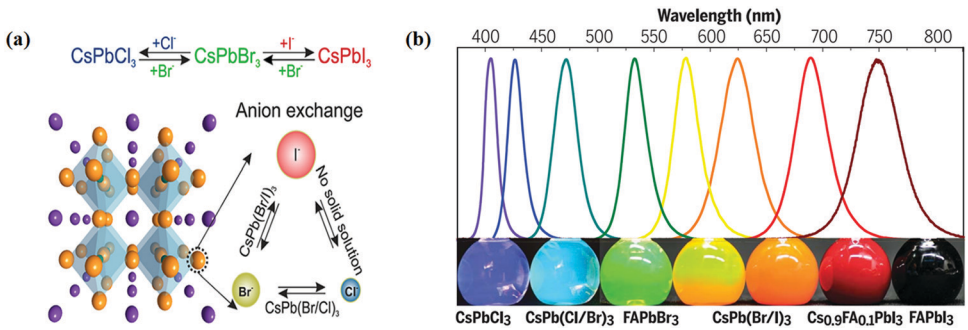

Fig. 5 (a) Schematic of the halide anion-exchange process. Reproduced with permission from ref. 38 at https://pubs.acs.org/doi/abs/10.1021/acs.nanolett.5b02404; further permissions are directed to the ACS. (b) Photoluminescence spectra and the corresponding photographs (under varied daylight and UV excitation) of colloid composition-tuned $APbX_3$ NCs. From ref. 92, reprinted with permission from AAAS.

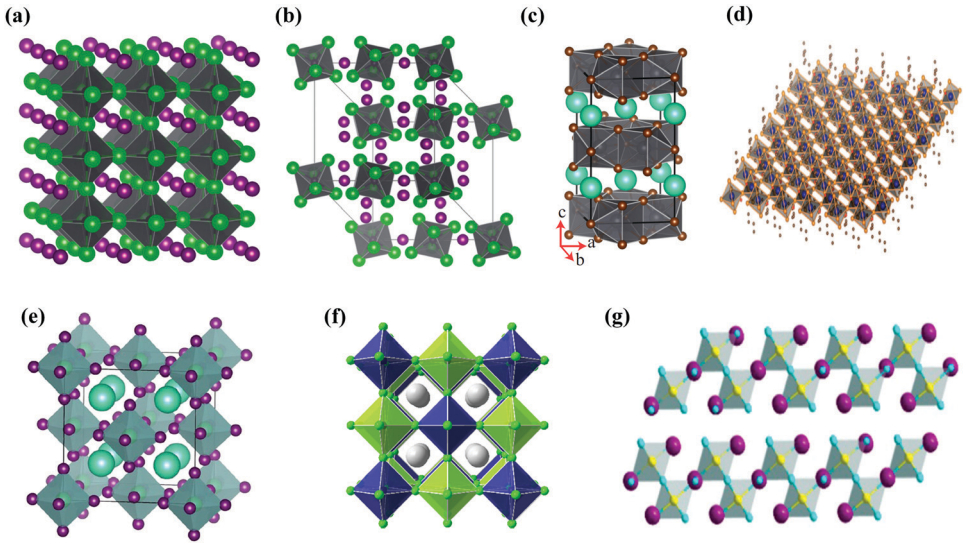

Fig. 6 Schematic illustration of different halide structures: (a) pseudocubic ABX_3 (3D) and (b) A_4BX_6 (reproduced with permission from ref. 115 at https://pubs.acs.org/doi/abs/10.1021/acs.nanolett.6b05262; further permissions are directed to the ACS); (c) AB_2X_5 (2D), reprinted with permission from ref. 116, Copyright 2017 by the American Physical Society; (d) A_2BX_4, from ref. 118, reprinted with permission from AAAS. (e) A_2BX_6 (0D), reproduced from ref. 120 under the Creative Commons CC BY license (https://creativecommons.org/licenses/by/4.0/); (f) $A_2B^+B^{3+}X_6$ (3D), reprinted with permission from ref. 123, Copyright 2016 American Chemical Society; (g) $A_3B_2X_9$ (2D), reprinted with permission from ref. 121, Copyright 2017 American Chemical Society.

research interest up to now. However, the inherent toxicity and overall reactivity of these halide perovskites have also motivated the scientists to investigate them in various research directions. Firstly, the structural instability and higher ionicity of LHP NCs could usually be taken as a positive aspect, as the $APbX_3$ lattice could be easily rationalized into other phases. This has motivated the researchers to investigate NCs more extensively by exploring their composition and structural characteristics that are defined as "perovskite-related structures", for example Cs_4PbX_6 and $CsPb_2X_5$ (often called zero-dimensional (0D) and two dimensional (2D) structures, respectively), whereas the characterization of the 3D $APbX_3$ structure was observed to have corner-sharing $[PbX_6]^{4-}$ octahedra with the A^+ cations filling the holes formed by four neighboring PbX_6^{4-} octahedra ensuing in a cubic or pseudo-cubic structure (Fig. 6a). The PbX_6^{4-} octahedra in A_4PbX_6 structures are dissociated in all extents and the halide ions are no longer shared between them (Fig. 6b).[114,115] Layered perovskites have recently been under a lot of scrutinization process. Similar to that of layered double hydroxides containing alternating Cs^+ and $[Pb_2X_5]^-$ polyhedron layers, the $CsPb_2X_5$ has emerged as a 2D version of lead halide perovskite materials with a tetragonal phase (Fig. 6c).[116,117] Another type that contains an alternating layer of corner-sharing $[PbX_6]^{4-}$ octahedra and bulky cations is known as the 2D perovskite A_2PbX_4 phase (Fig. 6d).[118]

In $APbX_3$ NC systems, the lead toxicity and its bioaccumulation in the ecosystem are known as key drawbacks, which in turn motivate the researchers to find alternative materials with similar optoelectronic characteristics, such as Cs_2SnI_6 NCs.[119–121] To date, there has been very little success. Cs_2SnI_6 crystallizes in the face-centered cubic structure. Four $[SnI_6]^{2-}$ octahedra at the corners and face centers and eight Cs_+ cations at the tetragonal interstitials make up the unit cell (Fig. 6e). A Cs_2SnI_6 structure is a perovskite derivative that is made by removing half of the Sn atoms at regular intervals from each center of the $[SnI_6]$ octahedron.[120] Because of this, the structure is also known as a "vacancy ordered double perovskite." Two primary techniques are now being explored in the search for lead-free metal halide compounds: a "simple" substitution of Pb^{2+} cations with other less toxic divalent metal ions from the same group IV, such as Sn or Ge, and a "complex" substitution of Pb^{2+} cations with other less toxic divalent metal ions from the same group IV,[122] such as Sn or Ge or a substitution of one monovalent M^+ and one trivalent M^{3+} cation for every two divalent Pb^{2+} ions (*i.e.*, $2Pb^{2+} \rightarrow B^+ + B^{3+}$), resulting in quaternary $A_2B^+B^{3+}X_6$ systems also known as "double perovskites" as shown in Fig. 6f.[123] Other transition or post-transition metals, like Fe^{3+} and Bi^{3+}, were used to examine the diversity of halide compounds associated with LHPs.[124–127] $Cs_3M_2X_9$ (M = Fe^{3+} and Bi^{3+}) crystallizes in the hexagonal space group $P6_3/mmc$. This is made up of isolated clusters, each of which is made up of two face-sharing octahedra and has the $M_2Br_9^{3-}$ formula, with Cs^+ acting as a bridging ion between the clusters. Antimony-based halide compounds, on the other hand, form in a layered shape with each $Sb_2Br_9^{3-}$ cluster sharing corners with three octahedra (Fig. 6g).[121]

4. Performance of photocatalytic CO_2 reduction

4.1. Reaction medium

The solvent plays a critical role in photocatalytic reactions. Halide perovskites are unstable in a polar solvent; therefore, extensive research studies have been accomplished to find a suitable medium for photocatalytic reduction of CO_2. Low-polar ethyl acetate was utilized as the solvent due to the higher solubility of CO_2, which guarantees durable stability for

$CsPbBr_3$ NCs.[42] Thereafter, various groups reported the boost in the selectivity of CO_2 conversion (99%) with the suppression of production of H_2, with the addition of a small amount of water (<50 μl) in ethyl acetate medium.[45,100,101,113] However, employing acetonitrile/water (0.3 vol%) mixture showed photocatalytic reduction of CO_2 with a high conversion rate (149 μmol g^{-1} h^{-1}) of CO_2 to CO, compared to the ethyl acetate/water (0.3 vol%) mixture upon light irradiation using $CsPbBr_3$ NCs combined with porous g-C_3N_4. Moreover, enhanced selectivity as well as productivity of the photocatalytic reduction of CO_2 was obtained with a high content of diluted water (1.2 vol%).[128]

Owing to several polarities, dielectric constant, and CO_2 solubility, the selection of solvents can exert a higher effect on the reaction rate and selectivity. The pairing of a robust co-catalyst is the key factor for enhancing the performance of photocatalysis. Meanwhile, it can not only separate the photogenerated electrons by the creation of a Schottky junction within the co-catalyst and photocatalyst to hinder the charge recombination, but also lower the kinetic bottlenecks in the activation of CO_2.[129,130] In the present case, the best nonaqueous solvent was ethyl acetate, which resulted in the reduction reaction of CO_2 with an electron yield rate of 2.74 μmol g^{-1} h^{-1} along with 95.2% selectivity. Furthermore, a photo-deposition of Pt co-catalyst boosts the electron yield rate to 5.66 μmol g^{-1} h^{-1}.[131] Numerous additional solvents such as toluene, benzene, *etc.* were also explored for photocatalytic reduction of CO_2 as a photocatalysis medium in halide perovskite NCs.[101] Besides, owing to reducing the formation of less active CO_2, higher hydration products and selectivity, solid-vapor CO_2 reduction systems also remain very attractive. Mu *et al.* utilized hexafluorobutyl methacrylate to protect cobalt-doped $CsPbBr_3/Cs_4PbBr_6$ NCs for the photoreduction of CO_2 in the aqueous medium. They adopted pure water as a solvent, where water was used as a sacrificial reductant and electron source. The content of 2% Co on the surface of the NCs (2%Co@$CsPbBr_3$/Cs_4PbBr_6) was employed to enhance the activity for photocatalytic reduction of CO_2.[93] They proposed that Co^{2+} acted as an active center to promote CO_2 absorption and accrued two electrons from $CsPbBr_3/Cs_4PbBr_6$; on account of that, the Co^{2+} center formed a Co-CO_2 complex and reacted with H^+ to facilitate the formation of CO.

4.2. Halide perovskites

4.2.1. ABX_3 structure. The conventional ABX_3 structure halide perovskites have various phases such as cubic,[132] monoclinic,[42] orthorhombic,[45] hexagonal,[98] *etc.* Recently, Xu *et al.* theoretically proved that $CsPbBr_3$ with a cubic phase is an active catalyst for photocatalytic reduction of CO_2 in the presence of benzene.[100] The usage of organic solvents makes it challenging to find out the product source. Meanwhile, organic solvents may have smaller molecules that support the final product. Research should be focused on the synthesis of water-stable $CsPbX_3$ NCs that can be utilized for catalytic reactions in water or other polar solvents. The water-resistance of $CsPbX_3$ will also encourage their application in various fields. Most of the reported photocatalytic reductions of CO_2 into CO and CH_4 were performed in the non-aqueous system employing orthorhombic-$CsPbBr_3$ NCs as photocatalysts. Guo *et al.* reported

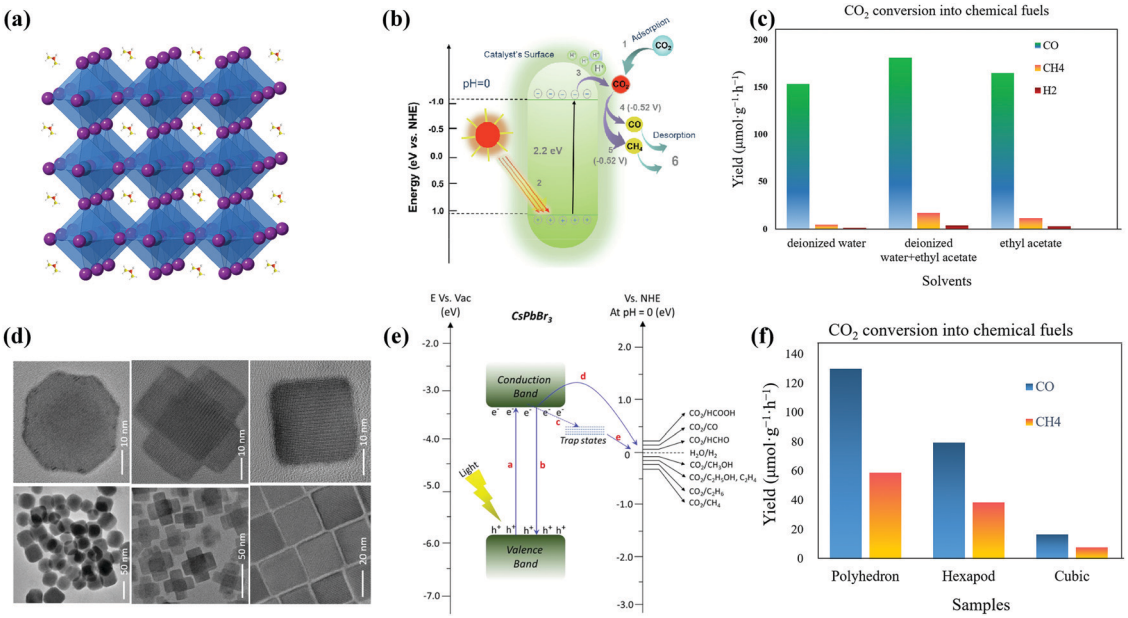

Fig. 7 (a) Crystal structure of the cubic $FAPbBr_3$ perovskite and (b) schematic band diagram of photocatalytic CO_2 reduction into chemical fuels for $FAPbBr_3$ QDs. Reprinted from ref. 51, Copyright 2021, with permission from Elsevier. (c) CO_2 reduction reaction by $FAPbBr_3$ QDs in DI, DI/EA, and EA systems (data from ref. 51). (d) TEM and HRTEM images of non-cubes, hexapods, and cube-shaped nanostructures. (e) Schematic representation of the conduction and valence band position of the $CsPbBr_3$ catalyst with the relative potential of CO_2 reduction. (d and e) Reprinted with permission from ref. 136, Copyright 2020 American Chemical Society. (f) Formation of CO and CH_4 from CO_2 reduction reactions using noncube, polyhedron, or hexapod photocatalysts (data from ref. 136).

that $CsPbBr_3$ with a cubic phase was more active than that with the orthorhombic ones because the phase transformation affects the efficiency of photocatalytic reduction of CO_2.[97] Recently, some perovskite materials with a uniform cubic shape, such as $FAPbBr_3$ QDs, have received much consideration owing to their long carrier recombination, along with the remarkable thermal, moisture, and illumination stabilities.[133,134] Que *et al.* developed $FAPbBr_3$ QDs with higher crystallinity as well as cubic shape by a hot injection method, which demonstrated high stability and the optimal yield of CO in the mixed solvent of ethyl acetate/deionized water. The results showed that $FAPbBr_3$ QD, as an alternative to halide perovskites, was a better reduction and capturing agent for CO_2 (Fig. 7a–c).[51] Bandgap and band position are the major parameters for efficient photocatalysts. Therefore, tuning the bandgap energy of halide perovskites could also improve the catalytic activity. Hou *et al.* reported that, from the view of the different quantum sizes of $CsPbBr_3$, 8.5 nm $CsPbBr_3$ NCs (~8.5 nm) achieved the optimal yields of CO, CH_4, and H_2 after 8 h of daylight illumination in an ethyl acetate/water medium.[135] For catalysis application, active facets for reacting species or products as well as the reduction of electron–hole recombination were facilitated for the efficient adsorption/desorption process. The highest production rate of CH_4 and CO was 7.6 and 16.4 μmol g^{-1}, respectively, for the $CsPbBr_3$ cubic shaped NCs, which matched well with the previously reported literature.[43,99,135] Conversely, the maximum activity was found to be higher for the hexapod nanostructures. The optimum yields of CH_4 and CO attained for hexapod NCs were 38.4 and 79.5 μmol g^{-1}, respectively, as compared to the 58.8 and 130.7 μmol g^{-1} for non-cubic NCs. The above-mentioned performance further demonstrated that poorly emitting non-cubic NCs that keep new facets showed a better photocatalytic activity as compared to the usual six-faceted cube nanostructures, as shown in Fig. 7d–f.[136]

4.2.2. Other structures. Lead-based halide perovskites are developing as the best encouraging type of materials for new-generation solar conversion energy.[137–139] The metal-based halide perovskite (MHP) NCs are proposed to solve the problem *via* the usage of organic photosensitizers, and to form highly effective photocatalytic systems. Despite the considerable success, the key problems of stability and toxicity are yet to be fixed. The photostability of metal-based halide perovskites is usually low in the presence of molecular oxygen (O_2).[140,141] The soft nature of MHP crystal lattices renders their surfaces prone to structural modification and degradation. Previous research has indicated that a partial or complete replacement of A site organic cations with Cs^+ can result in many new MHP compositions (all-inorganic chemical structure), which significantly promotes the photo- and humidity-stability.[142] Some studies have shown that the ionization energy can be used to predict the stability of perovskites. The ionization energy difference between cesium and methylammonium provides stability to all-inorganic HPs. For example, $CsPbBr_3$ nanocrystals are more stable in polar solvents, which is promising for a wide range of photo-redox catalysis reactions.[143]

Several approaches have been reported and applied to deal with the instability issues of MHPs. Examples include (i) replacing organic cations MA or FA with inorganic cations (*e.g.*, Cs^+);[144,145] (ii) creating heterostructures to spatially separate photogenerated excitons;[99] and (iii) encapsulating halide perovskites to minimize direct contact with highly polar environments.[45,93] In this context, the incident light absorption range for metallic complexes can be extended by coupling with

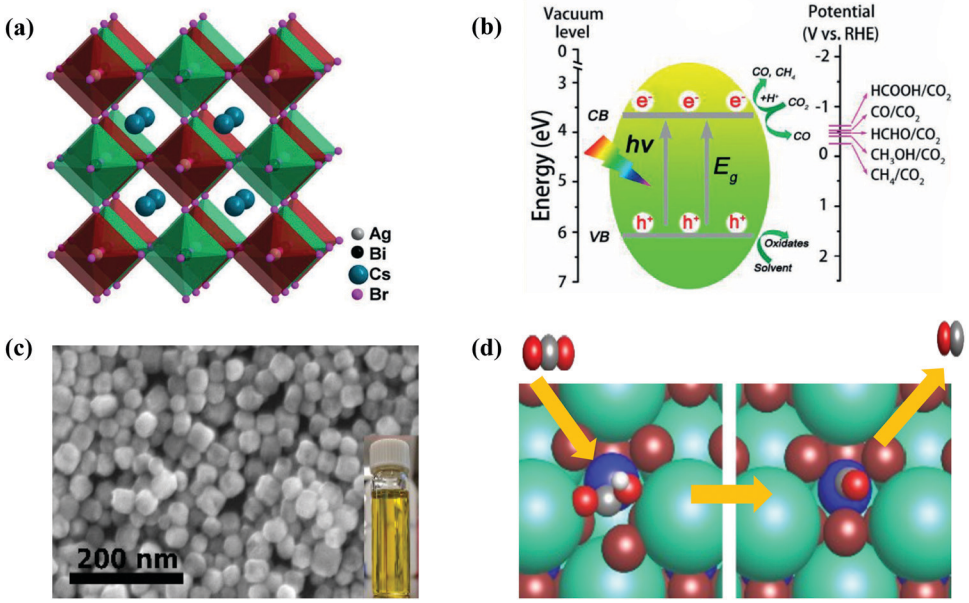

Fig. 8 (a) Crystal structure of cubic $Cs_2AgBiBr_6$. (b) Schematic diagram of the CO_2 photoreduction on the surface of $Cs_2AgBiBr_6$ NCs. (a and b) Reproduced with permission from ref. 44, Copyright 2018 Wiley. (c) SEM image of $Cs_3Sb_2Br_9$ NCs. The inset shows the yellow color and high transparency of the solution. (d) CO_2 reduction mechanism by $Cs_3Sb_2Br_9$ NCs. (c and d) Republished (adapted) with permission from the Royal Society of Chemistry from ref. 48; permission conveyed through Copyright Clearance Center, Inc.

halide perovskite NCs. Meanwhile, these metallic complexes are expected to be responsible for catalytic sites designed for halide perovskite NCs and capture excited electrons from halide perovskite NCs for selective photoreduction of CO_2. Lead-free inorganic halide double perovskites were based on antimony or bismuth and noble metals.[33] Most halide double perovskites have been described to have a cubic face-centered structure, which has the space group $Fm\bar{3}m$ and a lattice parameter ranging from approximately 10 to 12 Å.[123,146] This new type of perovskite consists of B'Cl_6 and B''Cl_6 octahedra alternating in a rock-salt face-centered cubic structure. George Volonakis *et al.*[147] used first-principles calculations to observe the patterns in the electronic and optical properties in the whole family of double halide perovskites, $A_2B'B''X_6$ with A = Cs; B″ = Bi and Sb; B′ = Cu, Ag, and Au; and X = Cl, Br, and I. Their calculations showed highly tunable carrier effective masses as well as optical gaps across the visible-light range of the electromagnetic spectra. Moving away from lead-based metal halide perovskites toward lead-free halide perovskites, Zhou *et al.* proved the photocatalytic reduction of CO_2 over double halide perovskite $Cs_2AgBiBr_6$ NCs in the presence of light in ethyl acetate.[44,148] The crystal structure of cubic $Cs_2AgBiBr_6$ NCs as well as constant advancement of CH_4 and CO on double halide perovskite $Cs_2AgBiBr_6$ NCs in the presence of solar light radiation is illustrated in Fig. 8(a and b). Lu *et al.* reported that substitution of unsaturated oleic acid with saturated octanoic acid was hazardous to synthesize pure $Cs_3Sb_2Br_9$ NCs without the CsBr contamination as shown in Fig. 8c.[48] $Cs_3Sb_2Br_9$ NCs showed much higher efficiency of photocatalytic reduction reaction of CO_2, compared to Pb-based $CsPbBr_3$ NCs. For photocatalytic reduction of CO_2, a bound state is observed for COOH* on the surface of $Cs_3Sb_2Br_9$ NCs in which a Br ion is partially replaced to allow for Sb–C bond formation as shown in Fig. 8d.[48] Dai *et al.* reported that the mesoporous silica-supported $Cs_3Bi_2Br_9$ NCs were developed. They observed that the $Cs_3Bi_2Br_9$ revealed outstanding photocatalytic properties in selective aromatic as well as non-aromatic C−H bond activation in the presence of sunlight.[149] Moreover, several environmentally friendly MHPs, such as $Cs_2InAgCl_6$,[150] $CsSnI_3$,[151] $Cs_3Sb_2I_9$,[152] and $Cs_3Sb_2Br_9$,[121] have been successfully produced. These metal-based HPs showed great optoelectronic properties for photocatalytic applications.

4.3. Semiconductors with halide perovskites

4.3.1. Oxide with halide perovskites. Inspired by the earth-abundant and nontoxic nature, TiO_2 has potential for application in CO_2 photoreduction. Hence, it is of significance to design a TiO_2 and perovskite-based heterojunction to enhance the photocatalytic reduction of CO_2. Xu *et al.* developed an S-scheme TiO_2/$CsPbBr_3$ heterojunction as a photocatalyst which showed higher activity for photocatalytic reduction of CO_2 into solar energies under UV-light radiation (Fig. 9a and b).[153] Xu *et al.* demonstrated novel amorphous-TiO_2-encapsulated $CsPbBr_3$ NCs for higher photocatalytic reduction of CO_2.[43] The amorphous TiO_2 encapsulation has been witnessed as a critical driving force for excellent photocatalytic performance through increasing the efficiency of

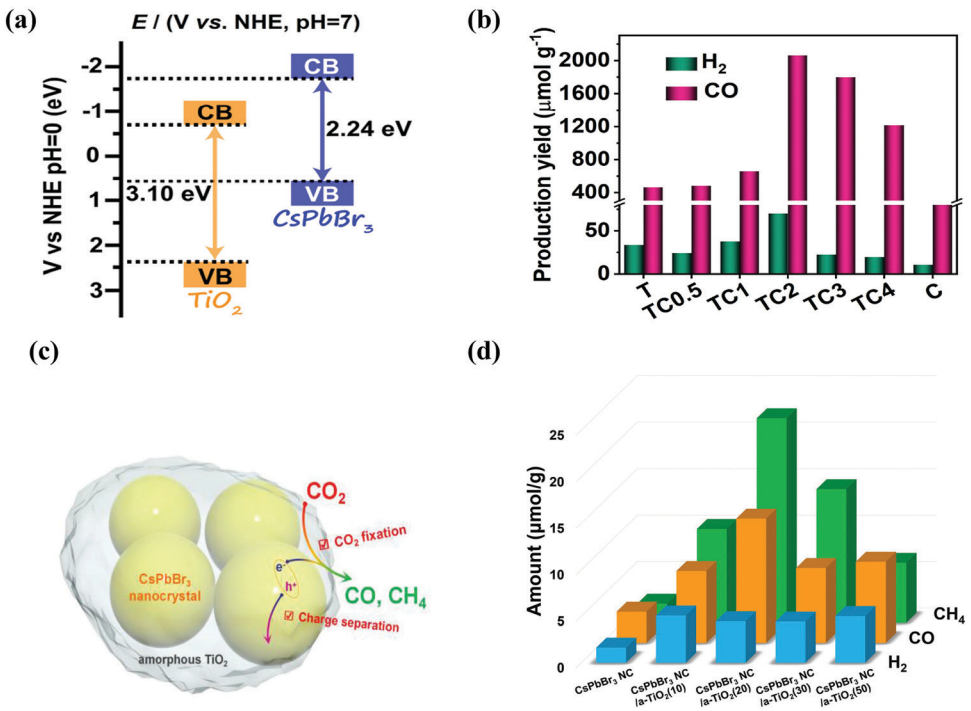

Fig. 9 (a) Band structure of the TiO_2/$CsPbBr_3$ composite photocatalyst. (b) Photocatalytic activities of CO_2 reduction for TiO_2, $CsPbBr_3$ QDs, and TiO_2/$CsPbBr_3$ composite, respectively. (a and b) Reproduced from ref. 153, under the Creative Commons CC BY license (http://creativecommons.org/licenses/by/4.0/). (c) A schematic illustration of CO_2 fixation and conversion in TiO_2-encapsulated $CsPbBr_3$ NCs, and (d) photocatalytic CO_2 reduction test results. (c and d) Reproduced with permission from ref. 43, Copyright 2018 Wiley.

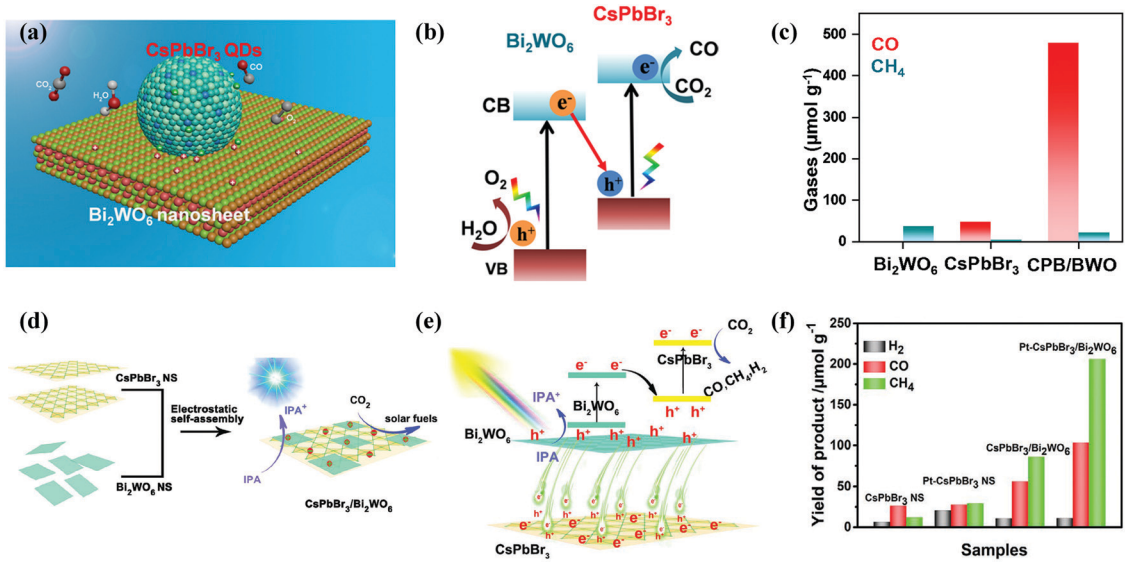

Fig. 10 (a) Z-Scheme photocatalytic diagram of the 0D/2D $CsPbBr_3/Bi_2WO_6$ composite for CO_2 reduction. (b) Schematic illustration of Z-scheme of the energy band structure of the $CsPbBr_3/Bi_2WO_6$ composite. (c) Gas yields in the ethyl acetate/water system over various catalysts. (a–c) Reprinted with permission from ref. 159, Copyright 2020 American Chemical Society. (d) Schematic diagram of the 2D/2D $CsPbBr_3/Bi_2WO_6$ heterojunction for CO_2 reduction. (e) Schematic diagram of the energy band structure of the 2D/2D $CsPbBr_3/Bi_2WO_6$ heterojunction. (f) Photocatalytic activity of different samples. (d–f) Reproduced with permission from ref. 167. Copyright 2020 Wiley.

extraction and separation of the photoinduced charges. Such effects finally enhanced the consumption of photoelectrons from 25.7 to 193.3 μmol g^{-1} as shown in Fig. 9c and d. Moreover, the adsorption and activation of CO_2 were also boosted. Based on these synergetic effects, an almost 6.5 times improvement in the consumption of the photoelectrons was attained through the photocatalytic CO_2 reduction reactions.[43]

When developing the stronger reduction potential of $CsPbBr_3$ to produce a Z-scheme heterojunction photocatalyst, it is best to search for a suitable oxidative semiconductor. Moreover, the oxidative semiconductor has the following properties: (i) strong interactions with $CsPbBr_3$; (ii) visible-light response; (iii) high catalytic activity for the oxidation reaction; and (iv) compatible band structure with $CsPbBr_3$. Bismuth tungsten oxide (Bi_2WO_6) is a unique oxide with visible-light response,[154] which contains perovskite-type $[WO_4]^{2-}$ layers and alternating $[Bi_2O_2]^{2+}$.[155,156] For oxidative reactions, Bi_2WO_6 also has an oxygen-deficient surface that provides abundant active sites, and it is preferred as an ideal photocatalyst for O_2 evolution.[157,158] Notably, the band structures among $CsPbBr_3$ and Bi_2WO_6 were well-matched, and in principle, they can also be incorporated into a Z-scheme heterojunction. Wang *et al.* developed a 0D/2D heterojunction of $CsPbBr_3$ QDs/Bi_2WO_6 nanosheet (CPB/BWO) photocatalyst for photocatalytic reduction of CO_2.[159] The larger surface area of 2D Bi_2WO_6 effectively decorated 0D $CsPbBr_3$ on its surface. The close contact between Bi_2WO_6 and $CsPbBr_3$ permitted an excellent interface for the charge transfer and separation.[160,161] The advanced CPB/BWO heterojunction photocatalyst exhibited higher activities for photocatalytic reduction of CO_2 as compared to the Bi_2WO_6 nanosheets and pristine $CsPbBr_3$ QDs (Fig. 10a–c), respectively.[159] The separated holes and electrons in $CsPbBr_3$ QDs and Bi_2WO_6 nanosheets can be proficiently used for photocatalytic reduction of CO_2. The yield of CPB/BWO is 503 μmol g^{-1}, which is 9.5 fold that of $CsPbBr_3$.

Besides, a 2D/2D heterojunction is considered as the most promising approach to manipulate the photoreduction efficiency of semiconductor catalysts. Recently, a lot of efforts have been devoted to preparing 2D/2D heterostructures.[162,163] This is because the large surface area of 2D ultrathin nanosheets, rich active sites, special electronic structure, and short charge transport distance are useful for the catalytic reaction.[164–166] Recently, Jiang *et al.* designed a lead halide perovskite-based 2D/2D direct Z scheme heterojunction by assembling ultrathin Bi_2WO_6 nanosheets on the surface of $CsPbBr_3$ nanosheets through an electrostatic self-assembly process (Fig. 10d–f).[167] Bi_2WO_6 has been identified as one of the best visible-light oxidation photocatalysts, which have higher oxidation ability, low manufacturing costs and controlled synthesis.[168,169] The $CsPbBr_3/Bi_2WO_6$ heterostructure provided higher photocatalytic performance for CO_2 reduction activity. The yield of the 2D/2D $CsPbBr_3/Bi_2WO_6$ hybrid was 153.0 μmol g^{-1} (10.9 μmol g^{-1} for H_2, 56.4 μmol g^{-1} for CO, and 86.0 μmol g^{-1} for CH_4).[167]

4.3.2. Sulfide with halide perovskites. A high-quality interface is strongly desired in heterojunctions for effectively separating electron–hole pairs both temporarily and spatially.[170] Co-sharing of atoms by two different materials in a heterojunction system could increase the charge separation and boost the carrier lifetime, facilitating the catalytic reaction. Recently, Wang *et al.* reported that 0D Cs_2SnI_6 QDs anchored on flower-like 2D SnS_2 nanosheets by co-sharing of Sn atoms can improve the photochemical CO_2 reduction rate.[46] All-inorganic Cs_2SnI_6 is favorable owing to its outstanding conductivity and strong chemical stability. For example, Cs_2SnI_6 thinner films have a high hole

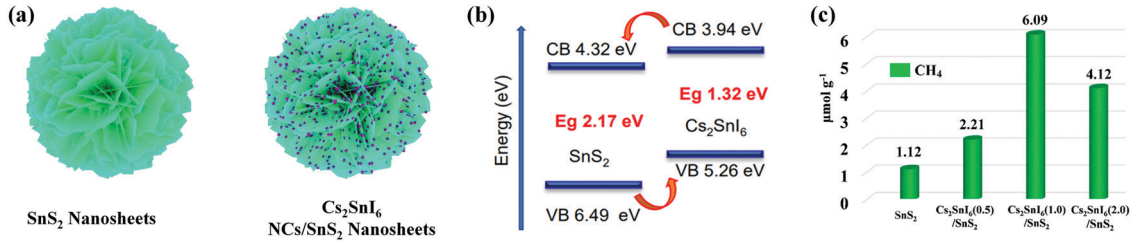

Fig. 11 (a) Schematic illustration of the synthesis of the Cs_2SnI_6/SnS_2 heterostructure. (b) Diagram of the energy band structure of Cs_2SnI_6 and SnS_2. (c) Comparison of photocatalytic CO_2 reduction activities of SnS_2, $Cs_2SnI_6(0.5)/SnS_2$, $Cs_2SnI_6(1.0)/SnS_2$, and $Cs_2SnI_6(2.0)/SnS_2$. Reprinted with permission from ref. 46, Copyright 2019 American Chemical Society.

mobility of 3.82×10^2 cm^2 V^{-1} s^{-1},[171] much larger than that of Si single crystals and $MAPbBr_3$ as a hole transport material.[172–176] In particular, the incorporation of Cs_2SnI_6 boosted the catalytic activity of SnS_2 owing to the facilitated charge separation. A flower-like Cs_2SnI_6/SnS_2 heterostructure was synthesized by dispersing the hydrothermally produced SnS_2 nanosheets in hydroiodic acid and ethanol alcohol (HI/EtOH) solution containing CsI, as shown in Fig. 11.[46] Joint research with DFT calculations, transient absorption, and kelvin probe force microscopy characterization proved a Cs_2SnI_6/SnS_2 hybrid having an intimate contact interface, which indicated that holes transferred from SnS_2 to Cs_2SnI_6 and electrons transferred from Cs_2SnI_6 to

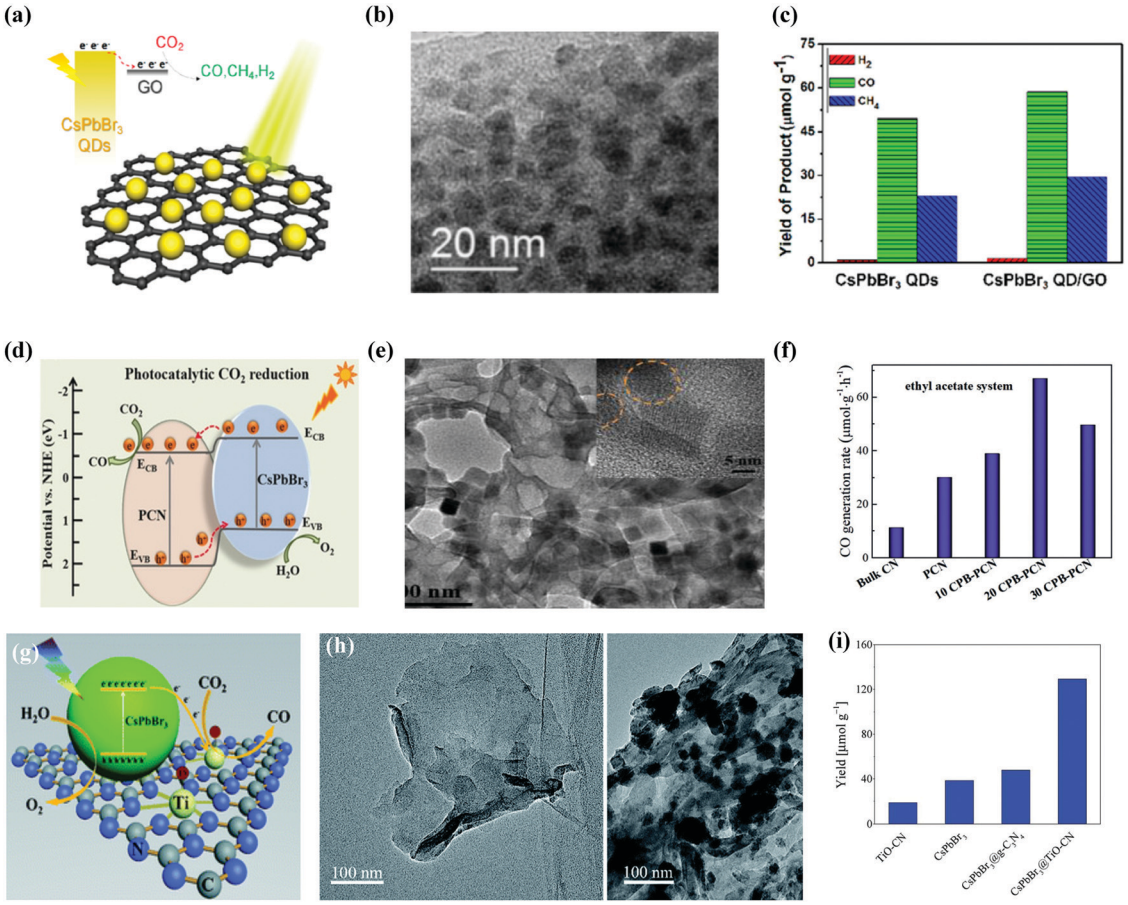

Fig. 12 Heterostructure of $CsPbBr_3$/GO composite photocatalysts for enhanced CO_2 reduction. (a) Schematic model, (b) TEM image, and (c) histogram of different products in the presence and absence of GO with $CsPbBr_3$ QDs. (a–c) Reprinted with permission from ref. 42, Copyright 2017 American Chemical Society. (d) Amino-assisted anchoring of $CsPbBr_3$ QDs on porous g-C_3N_4 for photocatalytic CO_2 reduction. (e) TEM image of $CsPbBr_3$-PCN. (f) Generation of CO in acetonitrile/water and ethyl acetate/water systems over various photocatalysts. (d–f) Reproduced with permission from ref. 182, Copyright 2018 Wiley. (g) Photocatalytic CO_2 reduction by $CsPbBr_3$ nanocrystals with graphitic carbon nitride nanosheets containing titanium-oxide composite. (h) TEM images of TiO-CN without and with $CsPbBr_3$ nanocrystals. (i) The yield of CO generation from photocatalytic CO_2 reduction reactions with TiO-CN, $CsPbBr_3$, $CsPbBr_3$@g-C_3N_4, and $CsPbBr_3$@TiO-CN. (g–i) Republished with permission of the Royal Society of Chemistry, from ref. 98; permission conveyed through Copyright Clearance Center, Inc.

SnS_2.[177] As a proof-of-concept application, photocatalytic reduction of CO_2 and photo-electrochemical experiments were conducted to demonstrate that the longer lifetime of accumulated electrons in SnS_2 boosted the performance by 5.4 times and 10.6 times compared to pristine SnS_2.[46]

4.3.3 Carbide with halide perovskites. Recently, carbon-based photocatalysts have aroused great concern and became more prevalent in photocatalytic reduction of CO_2 owing to their exceptional physicochemical and photo-/electrochemical properties. Various carbon materials (*e.g.* GO and g-C_3N_4) used as supports for many photocatalysts are greatly promising as carbon can regulate photocatalytic CO_2 reduction performance in the visible light region and extract photogenerated electrons from the surface of semiconductors because of its admirable electrical conductivity.[178–180]

Fig. 12a–c shows the representation of the $CsPbBr_3$ QD/GO composite photocatalyst and its corresponding TEM image.[42] It was noted that, in ethyl acetate, the pure $CsPbBr_3$ QDs catalyzed the photocatalytic reduction of CO_2 with an electron consumption rate of 23.75 μmol g^{-1} h^{-1} over 99.2% selectivity. Through the combination of highly conducting materials, such as GO, which has charge extraction abilities, the charge recombination was suppressed.[181] The $CsPbBr_3$ NCs/GO composite enhanced the electron consumption rate from 23.75 to 29.82 μmol g^{-1} h^{-1} with 99.15% selectivity.

Ou *et al.* described that anchoring of $CsPbBr_3$ QDs over porous g-C_3N_4 (PCN) also improved the performance of photocatalytic reduction of CO_2 in acetonitrile/water or ethyl acetate/water solution.[182] With 20 wt% $CsPbBr_3$ QDs (CPB) on NH_x-rich porous g-C_3N_4 nanosheets (CPB-PCN), $CsPbBr_3$ QDs were linked with PCN by a N-Br bond which boosted the photogenerated charge carrier separation, as shown in Fig. 12d–f.[182] The above-mentioned strategy helped to achieve the maximum rate of CO formation in the acetonitrile/water mixture compared with bare $CsPbBr_3$ QDs.[183]

Based on the above-mentioned composite structure, Guo *et al.* functionalized $CsPbBr_3$ NCs with graphitic carbon nitride, which had a titanium-oxide species (TiO-CN) through N–Br and O–Br bonding, and developed an effective catalyst system for photocatalytic reduction of CO_2 utilizing water as the source of electrons.[98] The introduction of TiO-CN could improve the number of catalytic active sites, along with a rapid interfacial charge separation between $CsPbBr_3$ and TiO-CN owing to their promising energy-offsets as well as chemical bonding performances (Fig. 12g–i). They also reported that the $CsPbBr_3$@TiO-CN composite increased the separation of photogenerated charges and improved the number of catalytic active sites that led to the formation of CO after 10 hours of irradiation, which was 3 times higher than that of pure $CsPbBr_3$.[98]

4.3.4 Metal–organic framework with halide perovskites. With unique structural architecture and admirable chemical and physical properties, metal–organic frameworks (MOFs) have recently attracted remarkable consideration regarding encapsulation of halide perovskites owing to their distinctive characteristics, such as tunable structure, higher surface areas, and flexibility.[184] Besides, zeolitic imidazolate framework (ZIF) based MOFs have shown great potential to capture CO_2, and cobalt possessing ZIFs can be co-catalysts to stimulate CO_2 activation and conversion.[185–187] Kong *et al.* described that the core@shell $CsPbBr_3$ NC@ZIF heterostructure boosted the yield

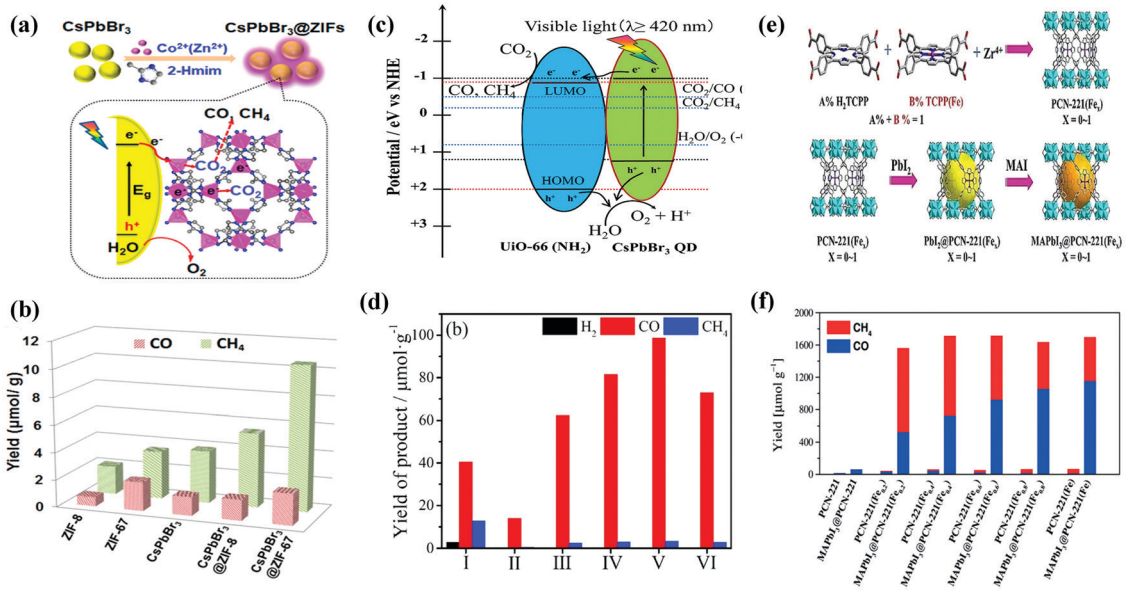

Fig. 13 (a) Schematic illustration of the fabrication process and CO_2 photoreduction process of $CsPbBr_3$/ZIFs. (b) The product yield after 3 h of photocatalytic reaction. (a and b) Reprinted with permission from ref. 102, Copyright 2018 American Chemical Society. (c) Schematic illustration of a possible mechanism of photocatalytic CO_2 reduction. (d) Photocatalytic CO_2 reduction performance for $CsPbBr_3$ QDs and *x*%-$CsPbBr_3$ QDs/UiO-66(NH_2) nanocomposite. (c and d) Reprinted from ref. 113, Copyright (2019), with permission from Elsevier. (e) Schematic representation for the synthesis of PCN-221(Fe_x) MOF and $MAPbI_3$@PCN221(Fe_x) composite photocatalysts for stable and product selective CO_2 reduction. (f) Histogram of product formation using PCN-221(Fe_x) and $MAPbI_3$@PCN-221(Fe_x). (e and f) Reproduced with permission from ref. 45, Copyright 2019 Wiley.

of photocatalytic reduction of CO_2.[102] The maximum quantity of CO_2 reduction yield was attained for the $CsPbBr_3$ NC@ZIF-67 composite with the highest electron consumption rate of 29.6 μmol g^{-1} h^{-1}, which was a 2.65 times increase compared to bare $CsPbBr_3$ NCs as shown in Fig. 13a and b. It was stated that $CsPbBr_3$ NCs covered by a ZIF shell can enhance the moisture stability and the CH_4 formation instead of CO as the main product.[102] Wan *et al.* developed a $CsPbBr_3$ NC/UiO-66(NH_2) composite toward the reduction of CO_2 in water/ethyl acetate with volume ratio (1/300) solution.[113] The highest conversion of CO_2 was accomplished for the 15%-$CsPbBr_3$ QD/UiO-66(NH_2) heterostructure.[113] The formation of CO was up to 98.5 μmol g^{-1}, which was higher as compared to the individual $CsPbBr_3$ QDs and UiO-66(NH_2) photocatalysts, as shown in Fig. 13c and d. The enhanced catalytic activity toward the reduction of CO_2 for the $CsPbBr_3$ QD/UiO-66(NH_2) composite was mainly ascribed to the creation of an appropriate band alignment of UiO-66(NH_2), which favored fast photogenerated electron transfer from the $CsPbBr_3$ QDs and repressed the charge recombination.[188–190] Lu and co-workers also demonstrated another promising application of MOF encapsulation, where Fe-porphyrin-based MOFs(PCN221(Fe_x)) secured $CH_3NH_3PbI_3$ ($MAPbI_3$) perovskite NCs in a reaction medium containing the maximum amount of H_2O (1.2 vol%) in ethyl acetate.[45] Fig. 13e and f shows that the $MAPbI_3$@PCN-221(Fe_x) composite photocatalyst shows the close contact of NCs and Fe photocatalytic site in the MOFs, favoring the rapid transfer of photogenerated electrons to the Fe catalytic sites and improving the performance of photoreduction.[42,102] The maximum yield of 1559 μmol g^{-1} was reported for the $MAPbI_3$@PCN-221(Fe 0.2) composite toward the photocatalytic reduction of CO_2 to CO (34.5%) and CH_4 (65.5%), where H_2O was used as an electron source.[45]

4.4. Conductor with halide perovskites

4.4.1. Noble Metal with halide perovskites. Recently the plasmon–exciton exchange dynamic method has been broadly suggested in metal–semiconductor systems. With the help from the famous localized surface plasmon resonance (LSPR) effect, noble metal Au nanoparticles (NP) were demonstrated by introducing light extinction into the visible and even near-infrared zone.[191,192] The $CsPbBr_3$–Au nanocomposite was successfully produced through the *in situ* reduction of $AuCl_3$ by the surface-bound oleylamine ligand, while the obtained Au NP size is too small to form the LSPR effect.[193,194]

Xiao and co-workers examined the energy conversion in the Ag-$CsPbBr_3$ system as well as dynamics of plasmon-induced hot electrons, which showed a significant hot-electron transfer efficiency near 50%.[195] The studies about plasmon-exciton interaction for the hybrid method of plasmonic Au NPs over halide perovskite NCs are still at a nascent development.

The $CsPbBr_3$–Au nanocomposite was used as a photocatalyst for artificial photoreduction of CO_2 by two different types of light sources ($\lambda > 420$ nm and $\lambda > 580$ nm). Based on the Kelvin probe force microscopy (KPFM) results and the spectroscopic characterization, two-dimensional interaction processes

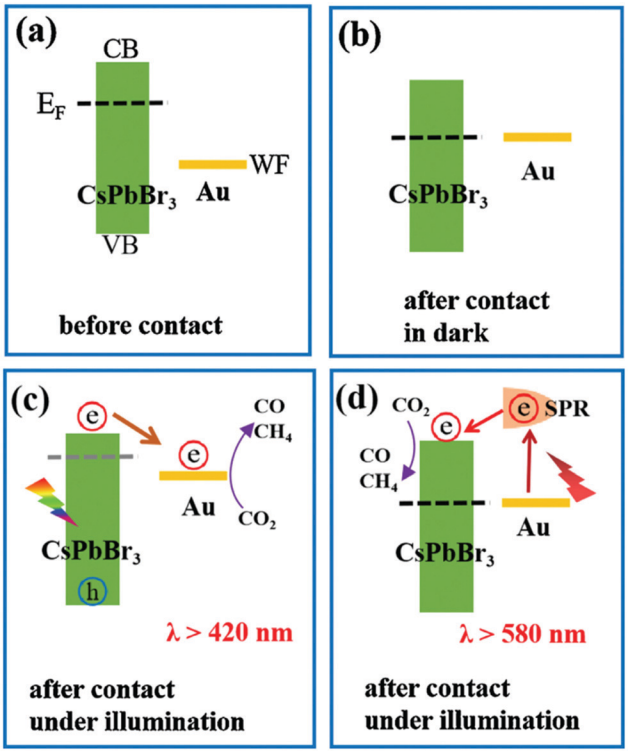

Fig. 14 (a) Band structure of $CsPbBr_3$ nanocrystals and Au nanoparticles before contact. (b) Fermi level alignment after their close contact in the dark. Schematic diagram of two excitation wavelength-dependent charge separation mechanisms in the $CsPbBr_3$–Au nanocomposite under light irradiation with (c) $\lambda > 420$ nm or (d) $\lambda > 580$ nm. (a–d) Reprinted from ref. 194, Copyright 2021, with permission from Elsevier.

for the $CsPbBr_3$–Au nanocomposite are shown in Fig. 14.[194] Even though there is a significant difference between the Fermi level (E_F) of $CsPbBr_3$ and the work function (W_F) of Au, energy level alignment can be obtained with their close contact (Fig. 14a and b). Consequently, photogenerated electrons would mostly accumulate in the CB of $CsPbBr_3$, which raises its E_F negatively, and thermodynamically supports the electrons to transfer into the Au.[196,197] The electrons accumulated in Au consequently contribute to the photoreduction reaction of CO_2, as demonstrated in Fig. 14c. Only the Au nanoparticle-based photo-responsive absorption occurred under the light condition of $\lambda > 580$ nm, while $CsPbBr_3$ based photo-responsive absorption started at wavelength $\lambda > 530$ nm. To initiate CO_2 reduction more efficiently, the LSPR-induced hot electrons encompassing higher energy potential in plasmonic Au nanoparticles could be further transferred rapidly to $CsPbBr_3$. Hence, this kind of plasmon-exciton exchange process makes the $CsPbBr_3$–Au nanocomposite work well over the longer wavelength in turn as shown in Fig. 14d.

Xu *et al.* described an innovative 0D $CsPbBr_3$ nanocrystal ($CsPbBr_3$ NC)/2D Pd nanosheet (Pd-NS) composite photocatalyst for the effective and stable photocatalytic reduction of CO_2 under sunlight in the existence of water vapor.[100] The Pd-NS not only played an important role as an electron collector to rapidly separate the electron–hole pairs in $CsPbBr_3$ NC and controlled the unwanted radiative charge recombination, but also modified

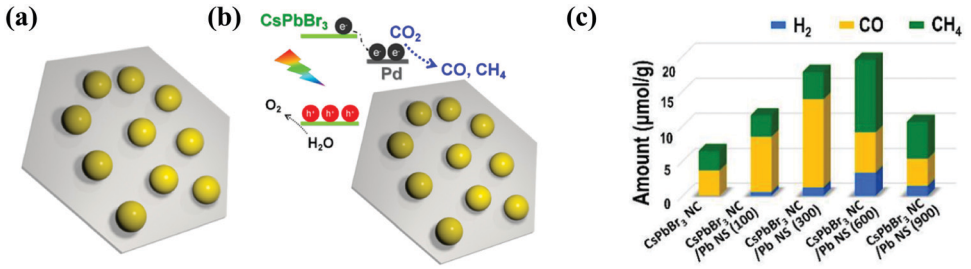

Fig. 15 (a) Diagram of the $CsPbBr_3$ NC/Pd-NC composite. (b) The sketch of the composite materials ($CsPbBr_3$ NC)/(Pd-NC) and their band alignments. (c) Photocatalytic CO_2 reduction performance. (a–c) Reprinted (adapted) with permission from ref. 100, Copyright 2018 American Chemical Society.

the kinetics of catalytic reduction of CO_2 reaction. Therefore, the addition of Pd-NS increased the consumption rate of photoelectrons from 9.85 μmol g^{-1} h^{-1} to 33.7 μmol g^{-1} h^{-1} under visible light (>420 nm);[100] especially, the incorporation of a 2D metallic semiconductor not only formed a Schottky junction at the interface to increase the electron transfer from the semiconductor to the metal, but also presented photocatalytic reaction sites to promote the transfer of electrons and increased the resulting chemical reactions,[164,198] as presented in Fig. 15a–c.

4.4.2. Carbon derivative with halide perovskites. Recently, 2D ultrathin carbon-based materials, such as carbon nanotubes (CNTs), graphene, and graphitic carbon nitride (g-C_3N_4), have drawn great attention toward photo/electrocatalytic applications. These materials possess the advantages of great metallic conductivity, strong volumetric capacitance, flexible interlayered regulation, hydrophilic surfaces,[199–203] tunable electronic structure, high surface area, excellent thermal/chemical stability, and environmental friendliness.[204,205] These properties have endorsed these materials to be employed in various applications, such as gas separation, cell imaging, catalysts, energy storage, and conversion.[206–208] Currently, some novel functional heterostructure for CO_2 reduction was prepared *via in situ* development of $CsPbBr_3$ perovskite NCs on 2D MXene nanosheets to further improve the charge transfer, separation, and effective photoexciton. The rapid charge transfer efficiency also encouraged the use of $CsPbBr_3$/MXene as an active catalyst towards the CO_2 conversion to CO and CH_4.[209] The low conduction band (1.5 eV) value among the $CsPbBr_3$ NCs and MXene can efficiently help the separation of the exciton in $CsPbBr_3$ NCs and electron transfer to MXene nanosheets. Photo-excitons will be shifted from a high energy level to a lower

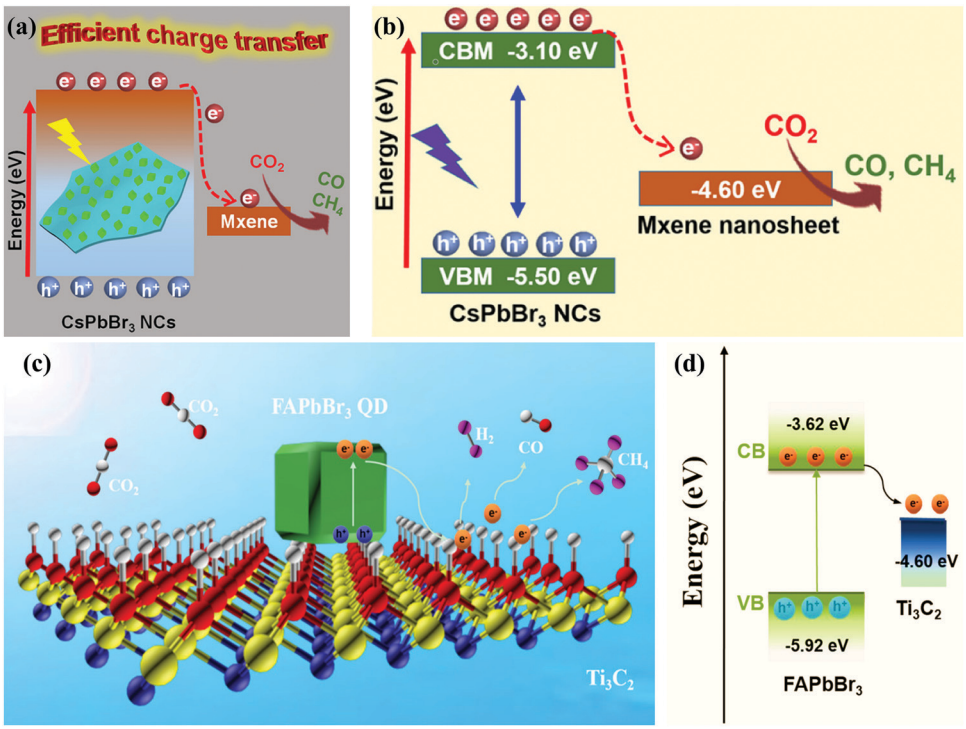

Fig. 16 (a) Schematic illustration and (b) the relative energy diagram of the $CsPbBr_3$ NC/MXene heterostructures suitable for photocatalytic CO_2 reduction. (a and b) Reprinted with permission from ref. 47, Copyright 2019 American Chemical Society. (c) Schematic diagram of the potential mechanism of photocatalytic CO_2 reduction in the $FAPbBr_3$/MXene composite. (d) Energy diagram of the band structure of $FAPbBr_3$/MXene. (c and d) Reprinted with permission from ref. 210, Copyright 2021 American Chemical Society.

one, therefore sustaining the charge at a stable state. In this way, electrons are moved to the surface of the photocatalyst, which offers a comparatively negative position based on the band arrangement.

Pan and co-workers demonstrated that the incorporation of MXene to $CsPbBr_3$ ($CsPbBr_3$ NCs/MXene-20) increased the yields of CO and CH_4 linearly. The maximum CH_4 and CO yield rate was 7.25 and 26.32 μmol g^{-1} h^{-1}, respectively (Fig. 16a and b),[47] which was superior or at least comparable to that of the MXene free $CsPbBr_3$ NCs (<4.42 μmol g^{-1} h^{-1}) or other state-of-the-art $CsPbBr_3$ NC-based heterostructure photocatalysts.[42,43,102,112,135,183] Que and co-workers successfully synthesized a $FAPbBr_3$ QD/MXene nanosheet heterostructure *via* a facile process. Under visible-light irradiation, the as-prepared $FAPbBr_3$ QD/MXene composite exhibited a remarkable photocatalytic activity in the presence of water. To stimulate the quick separation of excitons, the nanosheets of MXene played a role as an electron acceptor and facilitated a large number of active sites. Optimized performance with a higher electron consumption rate of 717.18 μmol g^{-1} h^{-1} was achieved *via* the $FAPbBr_3$ QD/MXene composite (Fig. 16c and d), which showed a 2.08 times better performance as compared to the pure $FAPbBr_3$ QDs.[210]

5. Molecular computation

Halide based perovskites have been extensively studied through theoretical/computational analysis concerning their unique electronic structure and physio-chemical properties. Their photo-conversion efficiency greatly depends on the balance electron, bandgap, absorption coefficient, hole mobility and intrinsic recombination rates.[211–213] Changes (element or molecular ion) in the structure of halide perovskites could significantly alter the optoelectronic properties. In many cases, replacing cations or anions in HPs may cause different Coulomb interaction which results in the shifting of conduction and valence band positions according to their Fermi level energy.[214] Bandgap is considered as one of the critical properties of a photocatalyst. To extend the light absorption to the visible region, the bandgap required for photocatalytic reaction is ~2.00 eV. However, the position of the conduction band minimum (CBM) should be lower than −0.52 eV (*vs.* NHE PH = 0, the energy barriers of reducing CO_2 to CO) for the CO_2 reduction reaction,[215,216] which is thermodynamically more feasible for the reduction reaction.

Liu and co-workers[217] conducted density functional theory (DFT) calculations of lead-free perovskites to investigate the valves of band gaps of $CsGeI_3$, $MAGeI_3$, and $FAGeI_3$ using exchange–correlation functionals. Some commonly used exchange–correlation functionals are Generalized Gradient Approximation (GGA) and Perdew–Burke–Ernzerhof (PBE) which were found to be consistent with experimental values. The same group also performed hybrid functional Heyd–Scuseria–Ernzerhof-06 (HSE06) calculations to obtain more precise values of band gaps, which were very close to experimental values. The optimized structures, calculated band structure, and density of states (DOS) of $MAGeI_3$ are shown in Fig. 17a–c. HSE06 and PBE functionals were used to calculate the bandgap of ABX_3 HPs, with and without spin orbit coupling (SOC) calculations.[218] Tang *et al.* elucidated the catalytic ability of pure $CsPbBr_3$ perovskite and doped $CsPbBr_3$ perovskites with different metals (Co, Fe, Ni, *etc.*) by density functional theory calculations.[139] It was shown that methane is formed with higher selectivity and the smaller band gap between Co-doped and Fe-doped perovskites improved the

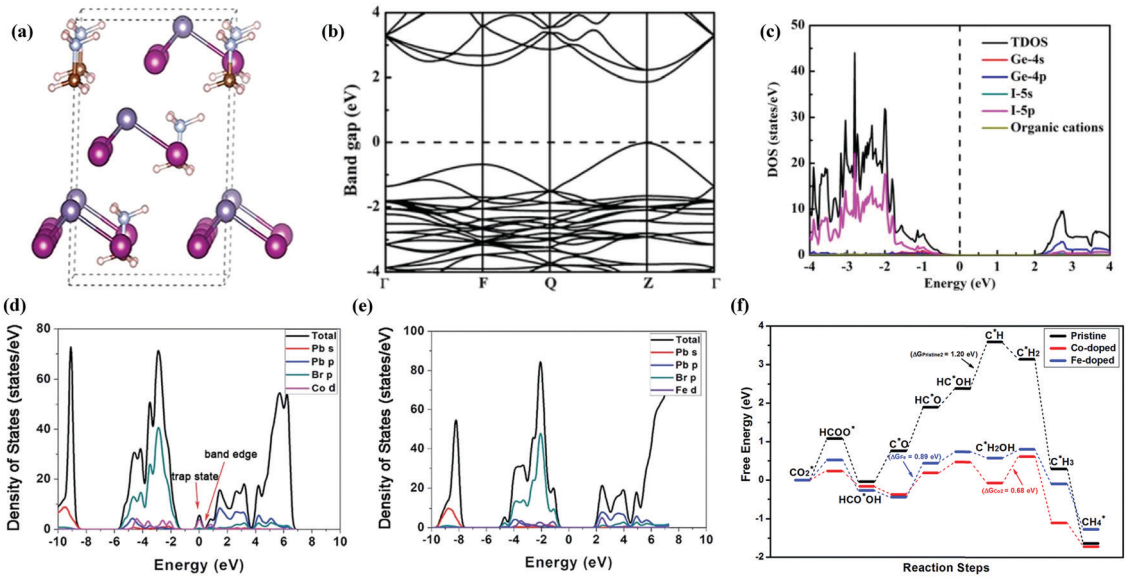

Fig. 17 (a) Optimized structure, (b) calculated band structure, and (c) DOS of $MAGeI_3$. Reprinted with permission from ref. 217, Copyright 2019 American Chemical Society. (d) Calculated density of state diagrams of Co-doped $CsPbBr_3$, (e) calculated density of state diagrams of Fe-doped $CsPbBr_3$, and (f) free-energy diagrams of the most favored paths of CO_2 reduction by pristine, Co-doped and Fe-doped $CsPbBr_3$. Republished with permission of the Royal Society of Chemistry, from ref. 139; permission conveyed through Copyright Clearance Center, Inc.

Table 2 Photocatalytic and CO_2 reduction performance using halide perovskites

Photocatalyst	Medium	Light source	Products	Yield (μmol g^{-1} h^{-1})	Highest efficiency (%)	Stability (h)	Ref.
$CsPbBr_3$ QDs	Ethyl acetate/water	300 W Xe lamp (AM 1.5G)	CO + CH_4 + H_2	4.3 + 1.5 + 0.1	—	>8	135
$CsPbBr_3$@g-C_3N_4	Ethyl acetate	450 W Xe lamp AM 1.5G	CO + CH_4	2.1 + 22.8	—	>12	220
$CsPb(Br_{0.5}/Cl_{0.5})_3$ NCs	Ethyl acetate	300 W Xe lamp (AM 1.5G)	CO + CH_4	85.2 + 12.0	—	>9	97
$CsPbBr_3$ QD/GO	Ethyl acetate	150 mW cm^{-2} (AM 1.5G)	CO + CH_4 + H_2	4.9 + 2.5 + 0.1	0.025	>12	42
$CsPbBr_3$@TiO-CN	Ethyl acetate/water	300 W Xe lamp ($\geq$400 nm)	CO	12.9	—	>10	98
$CsPbBr_3$ NCs/MXene	Ethyl acetate	300 W Xe lamp ($\geq$420 nm)	CO + CH_4	26.3 + 7.3	—	>9	47
$CsPbBr_3$ NCs/BZNW/MRGO	(CO_2 + water vapor)	150 W Xe lamp (AM 1.5G)	CO + CH_4	0.9 + 6.3	—	>3	99
$CsPbBr_3$ NCs/Pd NS	(CO_2 + water vapor)	150 W Xe lamp ($\geq$420 nm)	CO + CH_4 + H_2	1.9 + 3.5 + 1.1	0.035	>3	100
$CsPbBr_3$-Re(600)	Toluene/isopropanol	150 W Xe lamp ($\geq$420 nm)	CO + H_2	104.4 + 5.6	—	>3	101
$CsPbBr_3$ NCs/a-TiO_2	Ethyl acetate/isopropanol	150 W Xe lamp (AM 1.5G)	CO + CH_4 + H_2	3.9 + 6.7 + 1.5	—	>3	43
$CsPbBr_3$ NCs@ZIF-67	(CO_2 + water vapor)	150 mW cm^{-2} (AM 1.5G)	CO + CH_4	2.1 + 3.5	0.035	>3	102
$CsPbBr_3$ NCs@ZIF-8	(CO_2 + water vapor)	100 W Xe lamp (AM 1.5G)	CO + CH_4	0.7 + 2.0	—	>3	102
$CsPbBr_3$ QDs/UiO66(NH_2)	Ethyl acetate/water	300 W Xe lamp ($\geq$420 nm)	CO + CH_4	8.2 + 0.3	—	>12	113
$MAPbI_3$@PCN221(Fe_x)	Ethyl acetate/water	300 W Xe lamp ($\geq$400 nm) 100 mW cm^{-2}	CO + CH_4	4.2 + 13.0	—	25	45
Fe: $CsPbBr_3$ NCs	Ethyl acetate/water	450 W Xe lamp 150 mW cm^{-2}	CO + CH_4	3.2 + 6.1	—	>3	221
$FAPbBr_3/Bi_2WO_6$	Benzyl alcohol	150 W Xe lamp AM 1.5G 100 mW cm^{-2}	CO + Benzaldehyde	170.0 + 250.0	—	—	222
$FAPbBr_3$ QDs	Ethyl acetate/water	300 W Xe lamp 100 mW cm^{-2}	CO + CH_4 + H_2	181.3 + 16.9 + 2.37	—	>3	51
$CsPbBr_3$ QDs/Bi_2WO_6	Ethyl acetate/water	100 mW cm^{-2} > 400 nm	CO + CH_4	Totally 50.3	—	>10	159
Cs_2SnI_6/SnS_2 NCs	(CH_3OH + CO_2 + water vapor)	150 mW cm^{-2} ($\geq$400 nm)	CH_4	6.1	—	>3	46
$Cs_3Sb_2Br_9$	Octadecene	300 W Xe lamp 100 mW cm^{-2}	CO	127.2	—	>6	48
α-Fe_2O_3/Amine-RGO/$CsPbBr_3$	(CO_2 + water vapor)	150 W Xe lamp AM 1.5G, >420 nm	CO + CH_4 + H_2	2.4 + 9.5 + 0.3	—	>15	223
$CsPbBr_3$-Ni(tpy)	Ethyl acetate/water	300 W Xe lamp >400 nm 100 mW cm^{-2}	CO + CH_4	431.0 + 48.8	0.23	>4	50
$Cs_2AgBiBr_6$ NCs	Ethyl acetate	150 mW cm^{-2} (AM 1.5G)	CO + CH_4	2.4 + 1.6	0.028	>6	44
$Cs_3Bi_2I_9$	(CO_2 + water vapor)	80.38 μW cm^{-2} (AM 1.5G)	CO + CH_4	7.7 + 1.5	—	>10	224
$Co_{2\%}$@$CsPbBr_3$/Cs_4PbBr_6	Water	300 W Xe lamp 100 mW cm^{-2}	CO + CH_4	12.0 + 1.8	—	>20	225
Mn/$CsPb(Br/Cl)_3$	Ethyl acetate	300 W Xe-lamp with AM 1.5 filter	CO, CH_4	213, 9.1	—	9	226
Co-$CsPbBr_3$/Cs_4PbBr_6	Acetonitrile/water/Methanol	300 W Xe lamp 100 mW cm^{-2}	CO	122	—	15	227
Pt/$CsPbBr_3$	Ethyl acetate	150 W Xe-lamp with 380 nm cut o filter	CO	5.6	0.012	30	131
Ni and Mn-doped $CsPbCl_3$ NCs	(CO_2 + water vapor)	300 W Xe-lamp with AM 1.5 filter	Ni═CO Mn═CO	169.37, 152.49	—	6	228
Cs_4PbBr_6/rGO	Ethyl acetate/water	300 W Xe-lamp with 420 nm filter (light intensity, 100 mW cm^{-2})	CO	11.4	—	60	229
Cu-RGO-$CsPbBr_3$	(CO_2/water vapor)	Xe-lamp irradiation with a 400 nm filter	CH_4	12.7	(1.1 $\pm$ 0.15)	12	49
$TiO_2/CsPbBr_3$	Acetonitrile/water	300 W Xe-arc lamp	CO	9.02	—	16	153
$Cs_2AgBiBr_6$@g-C_3N_4	Ethyl acetate/Methanol	Xe-lamp (80 mW cm^{-2} light intensity)	CO, CH_4	2	—	12	52

efficiency of the photocatalyst as shown in Fig. 17f. The adsorption free energy of intermediates was found to be much lower than that of pure perovskite (Fig. 17f). Besides, the calculations also showed that the Co and Fe doped catalyst can enhance the catalytic activity of $CsPbBr_3$ towards CO_2 reduction. When dopants (Co or Fe) were introduced into $CsPbBr_3$, the band-edge states were created by Co-d and Fe-d orbitals as they contributed more actively to the CB. The formed band-edge states reduced the bandgap from 2.32 eV to 1.79 and 1.71 eV for Co-doped for Fe-doped cases, respectively. The reduced bandgap not only improved light absorption in the visible spectrum but also promoted effective charge separation and transfer efficiency.[139,219] Density of states was calculated as shown in Fig. 17d and e for the Co-doped and the Fe-doped cases respectively. The electron-donating ability of Co and Fe is greater than that of Pb, leading to improved reduction performance of doped HPs. Besides, calculation results showed that the C═O double bond becomes weaker for the Co-doped and Fe-doped structures and CO_2* is activated to produce HCOO*.[139]

6. Conclusion and future outlook

In this review, we summarize the recent progress achieved in exploring perovskite nanomaterials in terms of photocatalysts for CO_2 reduction. Improvement methods in this field are discussed systematically including utilizing newly emerging halide perovskite nanomaterials along with their modifications in terms of structural engineering, interfacial modulation through the formation of the heterostructure, metal ion

doping, surface modification, encapsulation with several types of co-catalysts, or using conducting substrates. Table 2 displays the performance of recent perovskite-based photocatalysts. Significant advances have been made to the conversion of CO_2 into useful energy-bearing hydrocarbons by many attractive approaches, while significant research effort is still needed for improvement in the field to accelerate practical implementation. Moreover, some fundamental studies are highly required to resolve the bottleneck problems, including the kinetic problem in multi-electron reduction processes, water oxidation reaction, poor reduction selectivity, and low quantum yield of the photocatalysts. These issues should be extensively examined and studied for future improvements to be employed on an industrial scale.

Promising research directions in halide perovskite-based photocatalysts for future exploration are forecasted including: (i) application of halide perovskites with various modulation strategies,[43,150,230,231] such as employing interface engineering, fabricating 3D hierarchical architectures, exploiting ultrathin 2D nanosheets, using the surface fluorination effects, preparing surfaces over layers, creating surface vacancies, *etc.* and (ii) accomplishing higher light-harvesting ability and enhancing charge separation efficiency *via* rational design of a novel halide perovskite-based heterostructure.[47,232–234] (iii) It's well known that solvent/electrolyte plays a significant role in any catalytic reaction. Since the halide perovskites are unstable in polar solvents, a wide range of research efforts have been devoted towards the exploration of a more suitable medium for efficient photocatalytic CO_2 reduction. Owing to the high solubility of CO_2, the use of low-polar ethyl acetate was preferred as a better solvent.[42] (iv) The utilization of co-catalysts in the photocatalytic process has been proved to be an environmentally benign method with high performance.[56] Some efforts could be devoted towards the development of an innovative noble-metal-free co-catalyst. (v) Despite attracting enormous research interest in the efficient photoreduction of CO_2, the use of halide perovskites is still restricted on the industrial scale owing to their low scale (μmol range). For artificial photosynthesis, the up to date solar-to-fuel efficiency value is $\sim$1.1%,[49] which is $\sim$10 times that of natural photosynthesis,[235] but is still very low for industrial applications. Given that solar energy conversion efficiency is $>$20% in solar photovoltaics, the value required for the feasible artificial photosynthesis should be 10% or above. The commercialization of CO_2 photoreduction reaction is currently obstructed by the poor stability, low selectivity and high cost. One promising way to address the challenge is combining the halide perovskite with other efficient semiconductors for improving charge separation capacity and optical behaviors, so as to enhance the catalytic efficiency and stability. Therefore, the development of long-lasting, cost-effective, and potentially scalable halide perovskites is highly required for a sustainable future. (vi) Doping with proper metal ions and altering the reaction system for obtaining multiple doped halide perovskites should also be proposed for the possible improvement of the photocatalytic performance and their stability for reduction reaction of CO_2. (vii) Another issue which should be addressed is the toxic nature of halide perovskites that hinders their commercial applications. In order to get environmentally friendly halide perovskites, substitution of lead (Pb) with other transition metals such as Sn, Sb and Bi is necessary. However, these transition metal substituted HPs have relatively poor stability as compared to Pb-based halide perovskites. Any further development of Pb-free HPs should address the limitations related to stability. (viii) In recent years, there has been an increasing amount of literature on photocatalytic reduction of CO_2 which focuses mainly on higher conversion rate of CO_2. The typical products of this photocatalytic reaction are single carbon atom compounds such as methane, carbon monoxide, formic acid, *etc.* However, current research in photocatalytic CO_2 reduction by halide perovskites has emphasized the productivity as well as selectivity of compounds with two or more carbons (C2+), for example, ethanol, ethane, acetic acid, *etc.*[87] Further research is required to investigate the productivity and selectivity of these C2+ products *via* photocatalytic reduction of CO_2 by halide perovskites to valuable products such as alkenes, aromatic hydrocarbons and alcohols, rather than less valuable products. These challenges we are facing could provide countless opportunities for further improvement in photocatalytic activity. We hope that the readers can get more new insights into the recent advancements and future directions toward the energy conversion applications of halide perovskites in the field of photocatalysis.

Conflicts of interest

The authors declare no competing financial interest.

Acknowledgements

This work was supported by the National Natural Science Foundation of China (12002271, 11872302, and 62004155), Scientific Research Project of Shaanxi Provincial Department of Education (20JK0714), Xi'an Science and Technology Plan Project, China (2019220914SYS024CG046), and Earth Engineering Center and Center for Advanced Materials for Energy and Environment at Columbia University.

References

1 X. Duan, J. Xu, Z. Wei, J. Ma, S. Guo, S. Wang, H. Liu and S. Dou, *Adv. Mater.*, 2017, **29**, 1701784.
2 H. He, M. Zhong, D. Konkolewicz, K. Yacatto, T. Rappold, G. Sugar, N. E. David, J. Gelb, N. Kotwal and A. Merkle, *Adv. Funct. Mater.*, 2013, **23**, 4720–4728.
3 Y. He, L. Zhang, B. Teng and M. Fan, *Environ. Sci. Technol.*, 2015, **49**, 649–656.
4 W. Zhang, A. R. Mohamed and W.-J. Ong, *Angew. Chem.*, 2020, **59**, 22894–22915.
5 J. H. Montoya, L. C. Seitz, P. Chakthranont, A. Vojvodic, T. F. Jaramillo and J. K. Nørskov, *Nat. Mater.*, 2017, **16**, 70–81.

6 J. L. White, M. F. Baruch, J. E. Pander III, Y. Hu, I. C. Fortmeyer, J. E. Park, T. Zhang, K. Liao, J. Gu and Y. Yan, *Chem. Rev.*, 2015, **115**, 12888–12935.
7 D. Kim, K. K. Sakimoto, D. Hong and P. Yang, *Angew. Chem., Int. Ed.*, 2015, **54**, 3259–3266.
8 P. V. Kamat, *J. Phys. Chem. C*, 2007, **111**, 2834–2860.
9 P. V. Kamat, *ACS Energy Lett.*, 2017, **2**, 1586–1587.
10 Ș. Neațu, J. A. Maciá-Agulló, P. Concepción and H. Garcia, *J. Am. Chem. Soc.*, 2014, **136**, 15969–15976.
11 T. Masson-Delmotte, P. Zhai, H. Pörtner, D. Roberts, J. Skea, P. Shukla, A. Pirani, W. Moufouma-Okia, C. Péan and R. Pidcock, *World Meteorological Organization*, Geneva, Tech. Rep, 2018.
12 E. Karamian and S. Sharifnia, *J. CO2 Util.*, 2016, **16**, 194–203.
13 H. Zhou, Y. Qu, T. Zeid and X. Duan, *Energy Environ. Sci.*, 2012, **5**, 6732–6743.
14 J. Wen, J. Xie, X. Chen and X. Li, *Appl. Surf. Sci.*, 2017, **391**, 72–123.
15 M. Ge, Q. Li, C. Cao, J. Huang, S. Li, S. Zhang, Z. Chen, K. Zhang, S. S. Al-Deyab and Y. Lai, *Adv. Sci.*, 2017, **4**, 1600152.
16 K. Li, A. D. Handoko, M. Khraisheh and J. Tang, *Nanoscale*, 2014, **6**, 9767–9773.
17 Q. A. Akkerman, G. Rainò, M. V. Kovalenko and L. Manna, *Nat. Mater.*, 2018, **17**, 394–405.
18 Z. Shi, S. Li, Y. Li, H. Ji, X. Li, D. Wu, T. Xu, Y. Chen, Y. Tian, Y. Zhang, C. Shan and G. Du, *ACS Nano*, 2018, **12**, 1462–1472.
19 H. Zai, C. Zhu, H. Xie, Y. Zhao, C. Shi, Z. Chen, X. Ke, M. Sui, C. Chen, J. Hu, Q. Zhang, Y. Gao, H. Zhou, Y. Li and Q. Chen, *ACS Energy Lett.*, 2018, **3**, 30–38.
20 F. Cao, D. Yu, X. Li, Y. Zhu, Z. Sun, Y. Shen, Y. Wu, Y. Wei and H. Zeng, *J. Mater. Chem. C*, 2017, **5**, 7441–7445.
21 Q. Chen, H. Zhou, Y. Fang, A. Z. Stieg, T.-B. Song, H.-H. Wang, X. Xu, Y. Liu, S. Lu, J. You, P. Sun, J. McKay, M. S. Goorsky and Y. Yang, *Nat. Commun.*, 2015, **6**, 7269.
22 K. Chen, X. Deng, G. Dodekatos and H. Tüysüz, *J. Am. Chem. Soc.*, 2017, **139**, 12267–12273.
23 Y. Wu, P. Wang, X. Zhu, Q. Zhang, Z. Wang, Y. Liu, G. Zou, Y. Dai, M. H. Whangbo and B. Huang, *Adv. Mater.*, 2018, **30**, 1704342.
24 G. Do Park, C. W. Lee and K. T. Nam, *Curr. Opin. Electrochem.*, 2018, **11**, 98–104.
25 X. Song, G. Wei, J. Sun, C. Peng, J. Yin, X. Zhang, Y. Jiang and H. Fei, *Nat. Catal.*, 2020, **3**, 1027–1033.
26 L.-F. Gao, W.-J. Luo, Y.-F. Yao and Z.-G. Zou, *Chem. Commun.*, 2018, **54**, 11459–11462.
27 A. Guerrero and J. Bisquert, *Curr. Opin. Electrochem.*, 2017, **2**, 144–147.
28 X. Li, J. Yu, M. Jaroniec and X. Chen, *Chem. Rev.*, 2019, **119**, 3962–4179.
29 E. A. Tsiwah, Y. Ding, Z. Li, Z. Zhao, M. Wang, C. Hu, X. Liu, C. Sun, X. Zhao and Y. Xie, *CrystEngComm*, 2017, **19**, 7041–7049.
30 D. M. Jang, D. H. Kim, K. Park, J. Park, J. W. Lee and J. K. Song, *J. Mater. Chem. C*, 2016, **4**, 10625–10629.
31 Z. Long, H. Ren, J. Sun, J. Ouyang and N. Na, *Chem. Commun.*, 2017, **53**, 9914–9917.
32 L. Protesescu, S. Yakunin, M. I. Bodnarchuk, F. Krieg, R. Caputo, C. H. Hendon, R. X. Yang, A. Walsh and M. V. Kovalenko, *Nano Lett.*, 2015, **15**, 3692–3696.
33 F. Zhang, H. Zhong, C. Chen, X. Wu, X. Hu, H. Huang, J. Han, B. Zou and Y. Dong, *ACS Nano*, 2015, **9**, 4533–4542.
34 L. Protesescu, S. Yakunin, O. Nazarenko, D. N. Dirin and M. V. Kovalenko, *ACS Appl. Nano Mater.*, 2018, **1**, 1300–1308.
35 J. Wang, J. Liu, Z. Du and Z. Li, *J. Energy Chem.*, 2021, **54**, 770–785.
36 C. Zhang, B. Wang, W. Li, S. Huang, L. Kong, Z. Li and L. Li, *Nat. Commun.*, 2017, **8**, 1138.
37 P. Fu, Q. Shan, Y. Shang, J. Song, H. Zeng, Z. Ning and J. Gong, *Sci. Bull.*, 2017, **62**, 369–380.
38 G. Nedelcu, L. Protesescu, S. Yakunin, M. I. Bodnarchuk, M. J. Grotevent and M. V. Kovalenko, *Nano Lett.*, 2015, **15**, 5635–5640.
39 D. Yang, M. Cao, Q. Zhong, P. Li, X. Zhang and Q. Zhang, *J. Mater. Chem. C*, 2019, **7**, 757–789.
40 Y. Chen, M. He, J. Peng, Y. Sun and Z. Liang, *Adv. Sci.*, 2016, **3**, 1500392.
41 S. Bonabi Naghadeh, B. Luo, G. Abdelmageed, Y.-C. Pu, C. Zhang and J. Z. Zhang, *J. Phys. Chem. C*, 2018, **122**, 15799–15818.
42 Y.-F. Xu, M.-Z. Yang, B.-X. Chen, X.-D. Wang, H.-Y. Chen, D.-B. Kuang and C.-Y. Su, *J. Am. Chem. Soc.*, 2017, **139**, 5660–5663.
43 Y. F. Xu, X. D. Wang, J. F. Liao, B. X. Chen, H. Y. Chen and D. B. Kuang, *Adv. Mater. Interfaces*, 2018, **5**, 1801015.
44 L. Zhou, Y. F. Xu, B. X. Chen, D. B. Kuang and C. Y. Su, *Small*, 2018, **14**, 1703762.
45 L. Y. Wu, Y. F. Mu, X. X. Guo, W. Zhang, Z. M. Zhang, M. Zhang and T. B. Lu, *Angew. Chem., Int. Ed.*, 2019, **58**, 9491–9495.
46 X.-D. Wang, Y.-H. Huang, J.-F. Liao, Y. Jiang, L. Zhou, X.-Y. Zhang, H.-Y. Chen and D.-B. Kuang, *J. Am. Chem. Soc.*, 2019, **141**, 13434–13441.
47 A. Pan, X. Ma, S. Huang, Y. Wu, M. Jia, Y. Shi, Y. Liu, P. Wangyang, L. He and Y. Liu, *J. Phys. Chem. Lett.*, 2019, **10**, 6590–6597.
48 C. Lu, D. S. Itanze, A. G. Aragon, X. Ma, H. Li, K. B. Ucer, C. Hewitt, D. L. Carroll, R. T. Williams and Y. Qiu, *Nanoscale*, 2020, **12**, 2987–2991.
49 S. Kumar, M. Regue, M. A. Isaacs, E. Freeman and S. Eslava, *ACS Appl. Energy Mater.*, 2020, **3**, 4509–4522.
50 Z. Chen, Y. Hu, J. Wang, Q. Shen, Y. Zhang, C. Ding, Y. Bai, G. Jiang, Z. Li and N. Gaponik, *Chem. Mater.*, 2020, **32**, 1517–1525.
51 M. Que, Y. Zhao, L. Pan, Y. Yang, Z. He, H. Yuan, J. Chen and G. Zhu, *Mater. Lett.*, 2021, **282**, 128695.
52 Y. Wang, H. Huang, Z. Zhang, C. Wang, Y. Yang, Q. Li and D. Xu, *Appl. Catal., B*, 2021, **282**, 119570.
53 H. Huang, B. Pradhan, J. Hofkens, M. B. J. Roeffaers and J. A. Steele, *ACS Energy Lett.*, 2020, **5**, 1107–1123.

54 J. Luo, W. Zhang, H. Yang, Q. Fan, F. Xiong, S. Liu, D.-S. Li and B. Liu, *EcoMat*, 2021, **3**, e12079.
55 C. B. Hiragond, N. S. Powar and S.-I. In, *Nanomaterials*, 2020, **10**, 2569.
56 S. Shyamal and N. Pradhan, *J. Phys. Chem. Lett.*, 2020, **11**, 6921–6934.
57 Y. Xu, M. Cao and S. Huang, *Nano Res.*, 2021, **14**, 3773–3794.
58 L. Li and M. Wang, Advanced Nanomatericals for Solar Photocatalysis, in *Advanced Catalytic Materials – Photocatalysis and Other Current Trends*, ed. L. E. Norena and J.-A. Wang, IntechOpen, 2016.
59 S. Linic, P. Christopher and D. B. Ingram, *Nat. Mater.*, 2011, **10**, 911–921.
60 F. Wang, Q. Li and D. Xu, *Adv. Energy Mater.*, 2017, **7**, 1700529.
61 L. Ran, J. Hou, S. Cao, Z. Li, Y. Zhang, Y. Wu, B. Zhang, P. Zhai and L. Sun, *Sol. RRL*, 2020, **4**, 2070045.
62 J. M. Elward and A. Chakraborty, *J. Chem. Theory Comput.*, 2013, **9**, 4351–4359.
63 F. Le Formal, S. R. Pendlebury, M. Cornuz, S. D. Tilley, M. Grätzel and J. R. Durrant, *J. Am. Chem. Soc.*, 2014, **136**, 2564–2574.
64 P. Zhou, J. Yu and M. Jaroniec, *Adv. Mater.*, 2014, **26**, 4920–4935.
65 H. Du, Y.-N. Liu, C.-C. Shen and A.-W. Xu, *Chin. J. Catal.*, 2017, **38**, 1295–1306.
66 M. Liu, Y. Pang, B. Zhang, P. De Luna, O. Voznyy, J. Xu, X. Zheng, C. T. Dinh, F. Fan, C. Cao, F. P. G. de Arquer, T. S. Safaei, A. Mepham, A. Klinkova, E. Kumacheva, T. Filleter, D. Sinton, S. O. Kelley and E. H. Sargent, *Nature*, 2016, **537**, 382–386.
67 X. Chen, S. Shen, L. Guo and S. S. Mao, *Chem. Rev.*, 2010, **110**, 6503–6570.
68 K. Sivula and R. van de Krol, *Nat. Rev. Mater.*, 2016, **1**, 15010.
69 W. Tu, Y. Zhou and Z. Zou, *Adv. Mater.*, 2014, **26**, 4607–4626.
70 Z. Li, J. Feng, S. Yan and Z. Zou, *Nano Today*, 2015, **10**, 468–486.
71 K. Li, X. An, K. H. Park, M. Khraisheh and J. Tang, *Catal. Today*, 2014, **224**, 3–12.
72 K. Li, B. Peng and T. Peng, *ACS Catal.*, 2016, **6**, 7485–7527.
73 J. H. Zejian Wang, S.-F. Ng, W. Liu, J. Huang, P. Chen and W.-J. Ong, *Acta Phys. - Chim. Sin*, 2021, **37**, 2011033.
74 J. Y. Choi, C. K. Lim, B. Park, M. Kim, A. Jamal and H. Song, *J. Mater. Chem. A*, 2019, **7**, 15068–15072.
75 Z. He, J. Zhang, X. Li, S. Guan, M. Dai and S. Wang, *Small*, 2020, **16**, 2005051.
76 W. Chen, B. Han, C. Tian, X. Liu, S. Liang, H. Deng and Z. Lin, *Appl. Catal., B*, 2019, **244**, 996–1003.
77 Z. Sun, Q. Fan, M. Zhang, S. Liu, H. Tao and J. Texter, *Adv. Sci.*, 2019, **6**, 1901084.
78 Z. Jiang, W. Wan, H. Li, S. Yuan, H. Zhao and P. K. Wong, *Adv. Mater.*, 2018, **30**, 1706108.
79 Y. Wang, S. Wang and X. W. D. Lou, *Angew. Chem., Int. Ed.*, 2019, **58**, 17236–17240.
80 H. Shen, T. Peppel, J. Strunk and Z. Sun, *Solar RRL*, 2020, **4**, 1900546.
81 P. Kar, S. Farsinezhad, N. Mahdi, Y. Zhang, U. Obuekwe, H. Sharma, J. Shen, N. Semagina and K. Shankar, *Nano Res.*, 2016, **9**, 3478–3493.
82 Y. Hori, H. Wakebe, T. Tsukamoto and O. Koga, *Electrochim. Acta*, 1994, **39**, 1833–1839.
83 Z. Sun, N. Talreja, H. Tao, J. Texter, M. Muhler, J. Strunk and J. Chen, *Angew. Chem., Int. Ed.*, 2018, **57**, 7610–7627.
84 R. Shi, G. I. Waterhouse and T. Zhang, *Sol. RRL*, 2017, **1**, 1700126.
85 X. Chang, T. Wang and J. Gong, *Energy Environ. Sci.*, 2016, **9**, 2177–2196.
86 S. C. Roy, O. K. Varghese, M. Paulose and C. A. Grimes, *ACS Nano*, 2010, **4**, 1259–1278.
87 J. Albero, Y. Peng and H. García, *ACS Catal.*, 2020, **10**, 5734–5749.
88 J. Wu, Y. Huang, W. Ye and Y. Li, *Adv. Sci.*, 2017, **4**, 1700194.
89 S. Wang, B. Y. Guan and X. W. D. Lou, *J. Am. Chem. Soc.*, 2018, **140**, 5037–5040.
90 Z. Fan, K. Sun and J. Wang, *J. Mater. Chem. A*, 2015, **3**, 18809–18828.
91 Y. Zhao and K. Zhu, *Chem. Soc. Rev.*, 2016, **45**, 655–689.
92 M. V. Kovalenko, L. Protesescu and M. I. Bodnarchuk, *Science*, 2017, **358**, 745–750.
93 Y. F. Mu, W. Zhang, X. X. Guo, G. X. Dong, M. Zhang and T. B. Lu, *ChemSusChem*, 2019, **12**, 4769–4774.
94 J. S. Manser, J. A. Christians and P. V. Kamat, *Chem. Rev.*, 2016, **116**, 12956–13008.
95 B. Saparov and D. B. Mitzi, *Chem. Rev.*, 2016, **116**, 4558–4596.
96 D. Weber, *Z. Naturforsch. B*, 1978, **33**, 1443–1445.
97 S.-H. Guo, J. Zhou, X. Zhao, C.-Y. Sun, S.-Q. You, X.-L. Wang and Z.-M. Su, *J. Catal.*, 2019, **369**, 201–208.
98 X.-X. Guo, S.-F. Tang, Y.-F. Mu, L.-Y. Wu, G.-X. Dong and M. Zhang, *RSC Adv.*, 2019, **9**, 34342–34348.
99 Y. Jiang, J.-F. Liao, Y.-F. Xu, H.-Y. Chen, X.-D. Wang and D.-B. Kuang, *J. Mater. Chem. A*, 2019, **7**, 13762–13769.
100 Y.-F. Xu, M.-Z. Yang, H.-Y. Chen, J.-F. Liao, X.-D. Wang and D.-B. Kuang, *ACS Appl. Energy Mater.*, 2018, **1**, 5083–5089.
101 Z.-C. Kong, H.-H. Zhang, J.-F. Liao, Y.-J. Dong, Y. Jiang, H.-Y. Chen and D.-B. Kuang, *Sol. RRL*, 2020, **4**, 1900365.
102 Z.-C. Kong, J.-F. Liao, Y.-J. Dong, Y.-F. Xu, H.-Y. Chen, D.-B. Kuang and C.-Y. Su, *ACS Energy Lett.*, 2018, **3**, 2656–2662.
103 J. Chen, J. Yin, X. Zheng, H. Ait Ahsaine, Y. Zhou, C. Dong, O. F. Mohammed, K. Takanabe and O. M. Bakr, *ACS Energy Lett.*, 2019, **4**, 1279–1286.
104 Q. Wang, L. Tao, X. Jiang, M. Wang and Y. Shen, *Appl. Surf. Sci.*, 2019, **465**, 607–613.
105 S. S. Bhosale, A. K. Kharade, E. Jokar, A. Fathi, S.-M. Chang and E. W.-G. Diau, *J. Am. Chem. Soc.*, 2019, **141**, 20434–20442.
106 M.-Z. Yang, Y.-F. Xu, J.-F. Liao, X.-D. Wang, H.-Y. Chen and D.-B. Kuang, *J. Mater. Chem. A*, 2019, **7**, 5409–5415.

107 M. I. Saidaminov, O. F. Mohammed and O. M. Bakr, *ACS Energy Lett.*, 2017, **2**, 889–896.
108 V. K. Ravi, G. B. Markad and A. Nag, *ACS Energy Lett.*, 2016, **1**, 665–671.
109 S. Yakunin, L. Protesescu, F. Krieg, M. I. Bodnarchuk, G. Nedelcu, M. Humer, G. De Luca, M. Fiebig, W. Heiss and M. V. Kovalenko, *Nat. Commun.*, 2015, **6**, 8515.
110 A. Filippetti and A. Mattoni, *Phys. Rev. B: Condens. Matter Mater. Phys.*, 2014, **89**, 125203.
111 Z. Zhu, Q. Sun, Z. Zhang, J. Dai, G. Xing, S. Li, X. Huang and W. Huang, *J. Mater. Chem. C*, 2018, **6**, 10121–10137.
112 D. Shi, V. Adinolfi, R. Comin, M. Yuan, E. Alarousu, A. Buin, Y. Chen, S. Hoogland, A. Rothenberger and K. Katsiev, *Science*, 2015, **347**, 519–522.
113 S. Wan, M. Ou, Q. Zhong and X. Wang, *Chem. Eng. J.*, 2019, **358**, 1287–1295.
114 Q. A. Akkerman, A. L. Abdelhady and L. Manna, *J. Phys. Chem. Lett.*, 2018, **9**, 2326–2337.
115 Q. A. Akkerman, S. Park, E. Radicchi, F. Nunzi, E. Mosconi, F. De Angelis, R. Brescia, P. Rastogi, M. Prato and L. Manna, *Nano Lett.*, 2017, **17**, 1924–1930.
116 F. Iyikanat, E. Sari and H. Sahin, *Phys. Rev. B*, 2017, **96**, 155442.
117 K. A. Huynh, D. L. T. Nguyen, V.-H. Nguyen, D.-V. N. Vo, Q. T. Trinh, T. P. Nguyen, S. Y. Kim and Q. V. Le, *J. Chem. Technol. Biotechnol.*, 2020, **95**, 2579–2596.
118 L. Dou, A. B. Wong, Y. Yu, M. Lai, N. Kornienko, S. W. Eaton, A. Fu, C. G. Bischak, J. Ma, T. Ding, N. S. Ginsberg, L. W. Wang, A. P. Alivisatos and P. Yang, *Science*, 2015, **349**, 1518–1521.
119 Y. Fu, H. Zhu, C. C. Stoumpos, Q. Ding, J. Wang, M. G. Kanatzidis, X. Zhu and S. Jin, *ACS Nano*, 2016, **10**, 7963–7972.
120 M. Faizan, K. C. Bhamu, G. Murtaza, X. He, N. Kulhari, M. M. Al-Anazy and S. H. Khan, *Sci. Rep.*, 2021, **11**, 6965.
121 J. Zhang, Y. Yang, H. Deng, U. Farooq, X. Yang, J. Khan, J. Tang and H. Song, *ACS Nano*, 2017, **11**, 9294–9302.
122 T. C. Jellicoe, J. M. Richter, H. F. J. Glass, M. Tabachnyk, R. Brady, S. E. Dutton, A. Rao, R. H. Friend, D. Credgington, N. C. Greenham and M. L. Böhm, *J. Am. Chem. Soc.*, 2016, **138**, 2941–2944.
123 E. T. McClure, M. R. Ball, W. Windl and P. M. Woodward, *Chem. Mater.*, 2016, **28**, 1348–1354.
124 F. Wei, F. Brivio, Y. Wu, S. Sun, P. D. Bristowe and A. K. Cheetham, *J. Mater. Chem. C*, 2018, **6**, 3573–3577.
125 Y. Zhang, J. Yin, M. R. Parida, G. H. Ahmed, J. Pan, O. M. Bakr, J.-L. Brédas and O. F. Mohammed, *J. Phys. Chem. Lett.*, 2017, **8**, 3173–3177.
126 B. Yang, J. Chen, F. Hong, X. Mao, K. Zheng, S. Yang, Y. Li, T. Pullerits, W. Deng and K. Han, *Angew. Chem., Int. Ed.*, 2017, **56**, 12471–12475.
127 Y. Hu, S. Zhang, X. Miao, L. Su, F. Bai, T. Qiu, J. Liu and G. Yuan, *Adv. Mater. Interfaces*, 2017, **4**, 1700131.
128 M. Ou, W. Tu, S. Yin, W. Xing, S. Wu, H. Wang, S. Wan, Q. Zhong and R. Xu, *Angew. Chem., Int. Ed.*, 2018, **57**, 13570.
129 W. Tu, Y. Xu, J. Wang, B. Zhang, T. Zhou, S. Yin, S. Wu, C. Li, Y. Huang and Y. Zhou, *ACS Sustainable Chem. Eng.*, 2017, **5**, 7260–7268.
130 J. Fu, K. Jiang, X. Qiu, J. Yu and M. Liu, *Mater. Today*, 2020, **32**, 222–243.
131 Y.-X. Chen, Y.-F. Xu, X.-D. Wang, H.-Y. Chen and D.-B. Kuang, *Sustainable Energy Fuels*, 2020, **4**, 2249–2255.
132 S. Thapa, K. Bhardwaj, S. Basel, S. Pradhan, C. J. Eling, A. M. Adawi, J.-S. G. Bouillard, G. J. Stasiuk, P. Reiss and A. Pariyar, *Nanoscale Adv.*, 2019, **1**, 3388–3391.
133 L. Protesescu, S. Yakunin, M. I. Bodnarchuk, F. Bertolotti, N. Masciocchi, A. Guagliardi and M. V. Kovalenko, *J. Am. Chem. Soc.*, 2016, **138**, 14202–14205.
134 I. Lignos, L. Protesescu, D. B. R. Emiroglu, R. Maceiczyk, S. Schneider, M. V. Kovalenko and A. J. deMello, *Nano Lett.*, 2018, **18**, 1246–1252.
135 J. Hou, S. Cao, Y. Wu, Z. Gao, F. Liang, Y. Sun, Z. Lin and L. Sun, *Chem. – Eur. J.*, 2017, **23**, 9481–9485.
136 S. Shyamal, S. K. Dutta, T. Das, S. Sen, S. Chakraborty and N. Pradhan, *J. Phys. Chem. Lett.*, 2020, **11**, 3608–3614.
137 S. De Wolf, J. Holovsky, S.-J. Moon, P. Löper, B. Niesen, M. Ledinsky, F.-J. Haug, J.-H. Yum and C. Ballif, *J. Phys. Chem. Lett.*, 2014, **5**, 1035–1039.
138 Y. Fu, H. Zhu, J. Chen, M. P. Hautzinger, X.-Y. Zhu and S. Jin, *Nat. Rev. Mater.*, 2019, **4**, 169–188.
139 C. Tang, C. Chen, W. Xu and L. Xu, *J. Mater. Chem. A*, 2019, **7**, 6911–6919.
140 G. Abdelmageed, L. Jewell, K. Hellier, L. Seymour, B. Luo, F. Bridges, J. Z. Zhang and S. Carter, *Appl. Phys. Lett.*, 2016, **109**, 233905.
141 N. Aristidou, C. Eames, I. Sanchez-Molina, X. Bu, J. Kosco, M. S. Islam and S. A. Haque, *Nat. Commun.*, 2017, **8**, 15218.
142 J.-W. Lee, D.-H. Kim, H.-S. Kim, S.-W. Seo, S. M. Cho and N.-G. Park, *Adv. Energy Mater.*, 2015, **5**, 1501310.
143 Y. Kim, E. Yassitepe, O. Voznyy, R. Comin, G. Walters, X. Gong, P. Kanjanaboos, A. F. Nogueira and E. H. Sargent, *ACS Appl. Mater. Interfaces*, 2015, **7**, 25007–25013.
144 S. You, S. Guo, X. Zhao, M. Sun, C. Sun, Z. Su and X. Wang, *Dalton Trans.*, 2019, **48**, 14115–14121.
145 Y. Jiang, J.-F. Liao, H.-Y. Chen, H.-H. Zhang, J.-Y. Li, X.-D. Wang and D.-B. Kuang, *Chem*, 2020, **6**, 766–780.
146 A. H. Slavney, T. Hu, A. M. Lindenberg and H. I. Karunadasa, *J. Am. Chem. Soc.*, 2016, **138**, 2138–2141.
147 G. Volonakis, M. Filip, A.-A. Haghighirad, N. Sakai, B. Wenger, H. Snaith and F. Giustino, *J. Phys. Chem. Lett.*, 2016, **7**, 1254–1259.
148 Z. Liu, H. Yang, J. Wang, Y. Yuan, K. Hills-Kimball, T. Cai, P. Wang, A. Tang and O. Chen, *Nano Lett.*, 2021, **21**, 1620–1627.
149 Y. Dai, C. Poidevin, C. Ochoa-Hernández, A. A. Auer and H. Tüysüz, *Angew. Chem., Int. Ed.*, 2020, **59**, 5788–5796.
150 G. Volonakis, A. A. Haghighirad, R. L. Milot, W. H. Sio, M. R. Filip, B. Wenger, M. B. Johnston, L. M. Herz, H. J. Snaith and F. Giustino, *J. Phys. Chem. Lett.*, 2017, **8**, 772–778.
151 I. Chung, J.-H. Song, J. Im, J. Androulakis, C. D. Malliakas, H. Li, A. J. Freeman, J. T. Kenney and M. G. Kanatzidis, *J. Am. Chem. Soc.*, 2012, **134**, 8579–8587.

152 J. Pal, S. Manna, A. Mondal, S. Das, K. V. Adarsh and A. Nag, *Angew. Chem., Int. Ed.*, 2017, **56**, 14187–14191.
153 F. Xu, K. Meng, B. Cheng, S. Wang, J. Xu and J. Yu, *Nat. Commun.*, 2020, **11**, 4613.
154 X.-F. Cao, L. Zhang, X.-T. Chen and Z.-L. Xue, *CrystEngComm*, 2011, **13**, 306–311.
155 H. Huang, R. Cao, S. Yu, K. Xu, W. Hao, Y. Wang, F. Dong, T. Zhang and Y. Zhang, *Appl. Catal., B*, 2017, **219**, 526–537.
156 C. Zhang and Y. Zhu, *Chem. Mater.*, 2005, **17**, 3537–3545.
157 Y. Zhou, Y. Zhang, M. Lin, J. Long, Z. Zhang, H. Lin, J. C.-S. Wu and X. Wang, *Nat. Commun.*, 2015, **6**, 8340.
158 J. Hu, D. Chen, Z. Mo, N. Li, Q. Xu, H. Li, J. He, H. Xu and J. Lu, *Angew. Chem., Int. Ed.*, 2019, **58**, 2073–2077.
159 J. Wang, J. Wang, N. Li, X. Du, J. Ma, C. He and Z. Li, *ACS Appl. Mater. Interfaces*, 2020, **12**, 31477–31485.
160 Q. Lu, Y. Yu, Q. Ma, B. Chen and H. Zhang, *Adv. Mater.*, 2016, **28**, 1917–1933.
161 D. Deng, K. Novoselov, Q. Fu, N. Zheng, Z. Tian and X. Bao, *Nat. Nanotechnol.*, 2016, **11**, 218–230.
162 J. Li, Y. Zhao, M. Xia, H. An, H. Bai, J. Wei, B. Yang and G. Yang, *Appl. Catal., B*, 2020, **261**, 118244.
163 Z. Xing, J. Hu, M. Ma, H. Lin, Y. An, Z. Liu, Y. Zhang, J. Li and S. Yang, *J. Am. Chem. Soc.*, 2019, **141**, 19715–19727.
164 C. Tan, X. Cao, X.-J. Wu, Q. He, J. Yang, X. Zhang, J. Chen, W. Zhao, S. Han and G.-H. Nam, *Chem. Rev.*, 2017, **117**, 6225–6331.
165 Y. Zhao, S. Zhang, R. Shi, G. I. Waterhouse, J. Tang and T. Zhang, *Mater. Today*, 2020, **34**, 78–91.
166 W. Wang, W. Zhao, H. Zhang, X. Dou and H. Shi, *Chin. J. Catal.*, 2021, **42**, 97–106.
167 Y. Jiang, H. Y. Chen, J. Y. Li, J. F. Liao, H. H. Zhang, X. D. Wang and D. B. Kuang, *Adv. Funct. Mater.*, 2020, 2004293.
168 N. Zhang, R. Ciriminna, M. Pagliaro and Y.-J. Xu, *Chem. Soc. Rev.*, 2014, **43**, 5276–5287.
169 H. Huang, C. Zhou, X. Jiao, H. Yuan, J. Zhao, C. He, J. Hofkens, M. B. Roeffaers, J. Long and J. A. Steele, *ACS Catal.*, 2019, **10**, 1439–1443.
170 P. Schulz, D. Cahen and A. Kahn, *Chem. Rev.*, 2019, **119**, 3349–3417.
171 G. Kapil, T. Ohta, T. Koyanagi, M. Vigneshwaran, Y. Zhang, Y. Ogomi, S. S. Pandey, K. Yoshino, Q. Shen and T. Toyoda, *J. Phys. Chem. C*, 2017, **121**, 13092–13100.
172 H. S. Rao, W. G. Li, B. X. Chen, D. B. Kuang and C. Y. Su, *Adv. Mater.*, 2017, **29**, 1602639.
173 Z. Chen, Q. Dong, Y. Liu, C. Bao, Y. Fang, Y. Lin, S. Tang, Q. Wang, X. Xiao and Y. Bai, *Nat. Commun.*, 2017, **8**, 1–7.
174 Y. Liu, J. Sun, Z. Yang, D. Yang, X. Ren, H. Xu, Z. Yang and S. Liu, *Adv. Opt. Mater.*, 2016, **4**, 1829–1837.
175 A. Kaltzoglou, M. Antoniadou, A. G. Kontos, C. C. Stoumpos, D. Perganti, E. Siranidi, V. Raptis, K. Trohidou, V. Psycharis and M. G. Kanatzidis, *J. Phys. Chem. C*, 2016, **120**, 11777–11785.
176 B. Lee, C. C. Stoumpos, N. Zhou, F. Hao, C. Malliakas, C.-Y. Yeh, T. J. Marks, M. G. Kanatzidis and R. P. Chang, *J. Am. Chem. Soc.*, 2014, **136**, 15379–15385.
177 X. Jiao, X. Li, X. Jin, Y. Sun, J. Xu, L. Liang, H. Ju, J. Zhu, Y. Pan, W. Yan, Y. Lin and Y. Xie, *J. Am. Chem. Soc.*, 2017, **139**, 18044–18051.
178 M. M. Kandy, *Sustainable Energy Fuels*, 2020, **4**, 469–484.
179 S. Zhang, Z. He, S. Xu, X. Li, J. Zhang, X. Zhan, M. Dai and S. Wang, *Solar RRL*, 2021, **5**, 2100233.
180 J. Low, B. Cheng, J. Yu and M. Jaroniec, *Energy Storage Mater.*, 2016, **3**, 24–35.
181 S. Kaniyankandy, S. Rawalekar and H. N. Ghosh, *J. Phys. Chem. C*, 2012, **116**, 16271–16275.
182 M. Ou, W. Tu, S. Yin, W. Xing, S. Wu, H. Wang, S. Wan, Q. Zhong and R. Xu, *Angew. Chem.*, 2018, **130**, 13758–13762.
183 C. Li, Y. Du, D. Wang, S. Yin, W. Tu, Z. Chen, M. Kraft, G. Chen and R. Xu, *Adv. Funct. Mater.*, 2017, **27**, 1604328.
184 C. Cao, D.-D. Ma, J.-F. Gu, X. Xie, G. Zeng, X. Li, S.-G. Han, Q.-L. Zhu, X.-T. Wu and Q. Xu, *Angew. Chem., Int. Ed.*, 2020, **59**, 15014–15020.
185 S. Wang, W. Yao, J. Lin, Z. Ding and X. Wang, *Angew. Chem., Int. Ed.*, 2014, **126**, 1052–1056.
186 J. Qin, S. Wang and X. Wang, *Appl. Catal., B*, 2017, **209**, 476–482.
187 S. Yan, S. Ouyang, H. Xu, M. Zhao, X. Zhang and J. Ye, *J. Mater. Chem. A*, 2016, **4**, 15126–15133.
188 L. Shen, S. Liang, W. Wu, R. Liang and L. Wu, *J. Mater. Chem. A*, 2013, **1**, 11473–11482.
189 G. Gao, Q. Xi, H. Zhou, Y. Zhao, C. Wu, L. Wang, P. Guo and J. Xu, *Nanoscale*, 2017, **9**, 12032–12038.
190 M. Kandiah, M. H. Nilsen, S. Usseglio, S. Jakobsen, U. Olsbye, M. Tilset, C. Larabi, E. A. Quadrelli, F. Bonino and K. P. Lillerud, *Chem. Mater.*, 2010, **22**, 6632–6640.
191 A. A. Zhumekenov, M. I. Saidaminov, M. A. Haque, E. Alarousu, S. P. Sarmah, B. Murali, I. Dursun, X.-H. Miao, A. L. Abdelhady and T. Wu, *ACS Energy Lett.*, 2016, **1**, 32–37.
192 G. Xing, N. Mathews, S. Sun, S. S. Lim, Y. M. Lam, M. Grätzel, S. Mhaisalkar and T. C. Sum, *Science*, 2013, **342**, 344–347.
193 J. Shamsi, A. S. Urban, M. Imran, L. De Trizio and L. Manna, *Chem. Rev.*, 2019, **119**, 3296–3348.
194 J.-F. Liao, Y.-T. Cai, J.-Y. Li, Y. Jiang, X.-D. Wang, H.-Y. Chen and D.-B. Kuang, *J. Energy Chem.*, 2021, **53**, 309–315.
195 X. Huang, H. Li, C. Zhang, S. Tan, Z. Chen, L. Chen, Z. Lu, X. Wang and M. Xiao, *Nat. Commun.*, 2019, **10**, 1163.
196 K. Wu, G. Liang, Q. Shang, Y. Ren, D. Kong and T. Lian, *J. Am. Chem. Soc.*, 2015, **137**, 12792–12795.
197 F. Liu, Y. Zhang, C. Ding, T. Toyoda, Y. Ogomi, T. S. Ripolles, S. Hayase, T. Minemoto, K. Yoshino, S. Dai and Q. Shen, *J. Phys. Chem. Lett.*, 2018, **9**, 294–297.
198 Z. Fan, X. Huang, C. Tan and H. Zhang, *Chem. Sci.*, 2015, **6**, 95–111.
199 M. Naguib, M. Kurtoglu, V. Presser, J. Lu, J. Niu, M. Heon, L. Hultman, Y. Gogotsi and M. W. Barsoum, *Adv. Mater.*, 2011, **23**, 4207.
200 B. Anasori, M. R. Lukatskaya and Y. Gogotsi, *Nat. Rev. Mater.*, 2017, **2**, 1–17.

201 S. Zhang, Z. He, X. Li, J. Zhang, Q. Zang and S. Wang, *Nanoscale Adv.*, 2020, **2**, 3610–3623.
202 R. Meng, J. Huang, Y. Feng, L. Zu, C. Peng, L. Zheng, L. Zheng, Z. Chen, G. Liu and B. Chen, *Adv. Energy Mater.*, 2018, **8**, 1801514.
203 H. Tao, Q. Fan, T. Ma, S. Liu, H. Gysling, J. Texter, F. Guo and Z. Sun, *Prog. Mater. Sci.*, 2020, **111**, 100637.
204 M. Arif, G. Yasin, M. Shakeel, M. A. Mushtaq, W. Ye, X. Fang, S. Ji and D. Yan, *J. Energy Chem.*, 2021, **58**, 237–246.
205 T. P. Nguyen, D. M. Tuan Nguyen, D. L. Tran, H. K. Le, D.-V. N. Vo, S. S. Lam, R. S. Varma, M. Shokouhimehr, C. C. Nguyen and Q. V. Le, *Mol. Catal.*, 2020, **486**, 110850.
206 Q. Xue, H. Zhang, M. Zhu, Z. Pei, H. Li, Z. Wang, Y. Huang, Y. Huang, Q. Deng and J. Zhou, *Adv. Mater.*, 2017, **29**, 1604847.
207 L. Ding, Y. Wei, L. Li, T. Zhang, H. Wang, J. Xue, L.-X. Ding, S. Wang, J. Caro and Y. Gogotsi, *Nat. Commun.*, 2018, **9**, 1–7.
208 M. Alhabeb, K. Maleski, T. S. Mathis, A. Sarycheva, C. B. Hatter, S. Uzun, A. Levitt and Y. Gogotsi, *Angew. Chem., Int. Ed.*, 2018, **130**, 5542–5546.
209 C. B. Hiragond, N. S. Powar and S.-I. In, *Nanomaterials*, 2020, **10**, 2569.
210 M. Que, Y. Zhao, Y. Yang, L. Pan, W. Lei, W. Cai, H. Yuan, J. Chen and G. Zhu, *ACS Appl. Mater. Interfaces*, 2021, **13**, 6180–6187.
211 X. Mao, L. Sun, T. Wu, T. Chu, W. Deng and K. Han, *J. Phys. Chem. C*, 2018, **122**, 7670–7675.
212 W.-J. Yin, J.-H. Yang, J. Kang, Y. Yan and S.-H. Wei, *J. Mater. Chem. A*, 2015, **3**, 8926–8942.
213 Y. Park and B. Park, *Results Phys.*, 2018, **11**, 302–305.
214 M. Irfan, S. Azam, S. Hussain, S. A. Khan, M. Sohail, M. Makhdoom, Z. Ali, I. V. Kityk, S. Muhammad and A. G. Al-Sehemi, *J. Alloys Compd.*, 2018, **766**, 536–545.
215 P. Kanhere and Z. Chen, *Molecules*, 2014, **19**, 19995–20022.
216 J. Schneider, H. Jia, J. T. Muckerman and E. Fujita, *Chem. Soc. Rev.*, 2012, **41**, 2036–2051.
217 D. Liu, Q. Li, H. Jing and K. Wu, *J. Phys. Chem. C*, 2019, **123**, 3795–3800.
218 S. T. A. G. Melissen, F. Labat, P. Sautet and T. Le Bahers, *Phys. Chem. Chem. Phys.*, 2015, **17**, 2199–2209.
219 X. Liu, J. Fan and C. Huang, *Front. Nanotechnol.*, 2021, **3**, 695490.
220 S. You, S. Guo, X. Zhao, M. Sun, C. Sun, Z. Su and X. Wang, *Dalton Trans.*, 2019, **48**, 14115–14121.
221 S. Shyamal, S. K. Dutta and N. Pradhan, *J. Phys. Chem. Lett.*, 2019, **10**, 7965–7969.
222 H. Huang, J. Zhao, Y. Du, C. Zhou, M. Zhang, Z. Wang, Y. Weng, J. Long, J. Hofkens and J. A. Steele, *ACS Nano*, 2020, **14**, 16689–16697.
223 Y. Jiang, J.-F. Liao, H.-Y. Chen, H.-H. Zhang, J.-Y. Li, X.-D. Wang and D.-B. Kuang, *Chem*, 2020, **6**, 766–780.
224 S. S. Bhosale, A. K. Kharade, E. Jokar, A. Fathi, S.-M. Chang and E. W.-G. Diau, *J. Am. Chem. Soc.*, 2019, **141**, 20434–20442.
225 Y.-F. Mu, W. Zhang, X.-X. Guo, G.-X. Dong, M. Zhang and T.-B. Lu, *ChemSusChem*, 2019, **12**, 4769–4774.
226 Y.-W. Liu, S.-H. Guo, S.-Q. You, C.-Y. Sun, X.-L. Wang, L. Zhao and Z.-M. Su, *Nanotechnology*, 2020, **31**, 215605.
227 G.-X. Dong, W. Zhang, Y.-F. Mu, K. Su, M. Zhang and T.-B. Lu, *Chem. Commun.*, 2020, **56**, 4664–4667.
228 J. Zhu, Y. Zhu, J. Huang, L. Hou, J. Shen and C. Li, *Nanoscale*, 2020, **12**, 11842–11846.
229 X. Wang, K. Li, J. He, J. Yang, F. Dong, W. Mai and M. Zhu, *Nano Energy*, 2020, **78**, 105388.
230 Z. Wang, H. Kim and H. N. Alshareef, *Adv. Mater.*, 2018, **30**, 1706656.
231 J. Song, L. Xu, J. Li, J. Xue, Y. Dong, X. Li and H. Zeng, *Adv. Mater.*, 2016, **28**, 4861–4869.
232 H. Huang, J. Li, Y. Yi, J. Wang, Y. Kang, P. K. Chu, H. Ong and X.-F. Yu, *Chem. Commun.*, 2018, **54**, 2365–2368.
233 R. Begum, M. R. Parida, A. L. Abdelhady, B. Murali, N. M. Alyami, G. H. Ahmed, M. N. Hedhili, O. M. Bakr and O. F. Mohammed, *J. Am. Chem. Soc.*, 2017, **139**, 731–737.
234 W. Deng, H. Huang, H. Jin, W. Li, X. Chu, D. Xiong, W. Yan, F. Chun, M. Xie and C. Luo, *Adv. Opt. Mater.*, 2019, **7**, 1801521.
235 Y. Shiraishi, T. Hagi, M. Matsumoto, S. Tanaka, S. Ichikawa and T. Hirai, *Commun. Chem.*, 2020, **3**, 169.